



Processes leading to deep convection and sensitivity to sea-state representation during HyMeX IOP8 heavy precipitation event

Marie-Noëlle Bouin, Jean-Luc Redelsperger, Cindy Lebeaupin Brossier

► To cite this version:

Marie-Noëlle Bouin, Jean-Luc Redelsperger, Cindy Lebeaupin Brossier. Processes leading to deep convection and sensitivity to sea-state representation during HyMeX IOP8 heavy precipitation event. Quarterly Journal of the Royal Meteorological Society, 2017, 143 (707), pp.2600-2615. 10.1002/qj.3111 . meteo-02108929

HAL Id: meteo-02108929

<https://meteofrance.hal.science/meteo-02108929>

Submitted on 24 Apr 2019

HAL is a multi-disciplinary open access archive for the deposit and dissemination of scientific research documents, whether they are published or not. The documents may come from teaching and research institutions in France or abroad, or from public or private research centers.

L'archive ouverte pluridisciplinaire **HAL**, est destinée au dépôt et à la diffusion de documents scientifiques de niveau recherche, publiés ou non, émanant des établissements d'enseignement et de recherche français ou étrangers, des laboratoires publics ou privés.



Processes leading to deep convection and sensitivity to sea-state representation during HyMeX IOP8 heavy precipitation event

Journal:	<i>QJRMS</i>
Manuscript ID	QJ-16-0348.R3
Wiley - Manuscript type:	Research Article
Date Submitted by the Author:	16-Jun-2017
Complete List of Authors:	Bouin, Marie-Noëlle; Météo France, CNRM; CNRS, Ifremer, IRD, UBO, LOPS Redelsperger, Jean-Luc; CNRS, Ifremer, IRD, UBO, LOPS LEBEAUPIN BROSSIER, Cindy; Météo-France/CNRS, CNRM
Keywords:	heavy precipitation event, HyMeX, mesoscale convective system, sea state, Mediterranean Sea, air-sea exchanges, cold pool, deep convection

1
2
3
4
5
6
7
8
9
10
11
12
13
14
15
16
17
18
19
20
21
22
23
24
25
26
27
28
29
30
31
32
33
34
35
36
37
38
39
40
41
42
43
44
45
46
47
48
49
50
51
52
53
54
55
56
57
58
59
60

Processes leading to deep convection and sensitivity to sea-state representation during HyMeX IOP8 heavy precipitation event

M.-N. Bouin^{1,2}, J.-L. Redelsperger², C. Lebeaupin Brossier¹

¹CNRM, UMR 3589, Météo-France & CNRS, Toulouse, France

²CNRS, Ifremer, IRD, UBO /Laboratoire d'Océanographie Physique et Spatiale (LOPS), UMR 6523, IUEM, Plouzané, France.

ABSTRACT

During the first observation period of the HyMeX programme, the Mediterranean coasts of Spain were impacted by several heavy precipitating events (HPEs). The most damaging one occurred during IOP 8 resulting in cumulative rainfall amount over 180 mm in the area of Murcia-Valencia. Numerical simulations using a high-resolution atmospheric model provide a very realistic representation of the mesoscale convective systems (MCSs) at the origin of this HPE and of the associated low-level conditions, consisting in two cold sectors surrounding a warm sector. This study provides a detailed analysis of the mechanisms of deep convection initiation and maintenance between 1200 UTC on 28 September and 0000 UTC on 29 September 2012. On the coastal mountainous area, the conditionally unstable inflow feeding the MCS is uplifted by the relief whereas at sea, a strong low-level convergence plays the same role. At the coast, cold pools are generated and strengthened by a strong low-level jet (LLJ) carrying cold dense air parcels from the Gulf of Lion and by evaporation and cooling under the precipitating systems. These cold pools play a key role in triggering the deep convection, either by directly uplifting the air masses or by deflecting horizontally the inflow. They largely control the localisation and distribution of the heavy

precipitation at sea near Valencia. A weak barrier wind over the cold pools and a secondary cyclonic circulation result in a bending of the convergence line at sea, in agreement with radar observations.

A sensitivity study to a more realistic representation of the sea state in the air-sea exchanges shows that the LLJ is decelerated by the increased sea-surface roughness, resulting in cold pools extending further at sea and shifting the precipitation patterns 50 km offshore.

Keywords: *heavy precipitation event; HyMeX; mesoscale convective system; sea state; Mediterranean Sea; air-sea exchanges; cold pool; deep convection*

1. Introduction

Heavy precipitation events (HPEs) affect regularly the western Mediterranean coastal regions in autumn and result often in flash flooding and landslides susceptible to produce thousands of millions euros damages and even casualties (e.g. Ricard *et al.*, 2012; Llasat *et al.*, 2013). Daily rainfall cumulative amounts higher than 150 mm are frequently observed as generated by multi-cell quasi-stationary mesoscale convective systems (MCSs; e.g. Ducrocq *et al.*, 2008; Buzzi *et al.*, 2014). These MCSs generally develop on the eastern edge of an upper-level trough extending from the British Isles to off the Iberian Peninsula associated with potential vorticity anomaly likely to generate low-level instability (Nuissier *et al.*, 2011; Duffourg *et al.*, 2016). A major ingredient common to all HPEs is the conditionally unstable moist marine flow extracting energy from the western Mediterranean sea surface, which is at its warmest in autumn and acts as a heat and moisture reservoir. This flow is directed towards the Spanish, Italian or French mountainous coastal regions where it undergoes continuously renewed lifting: the same local mechanisms enable uplifting at the same place. This lifting marks the onset of deep convection and precipitation on the coastal areas, and is a key ingredient of quasi stationarity. The complexity of the mountainous terrain and coastal topography has been demonstrated to be a factor influencing the orographic

1
2
3
4
5
6
7
8
9
10
11
12
13
14
15
16
17
18
19
20
21
22
23
24
25
26
27
28
29
30
31
32
33
34
35
36
37
38
39
40
41
42
43
44
45
46
47
48
49
50
51
52
53
54
55
56
57
58
59
60

triggering of the convection, along with the characteristics of the low-level inflow (Miglietta and Rotunno, 2010; 2012; Bresson *et al.*, 2012). The precise role of the relief in determining the location and distribution of the heavy precipitation has been recently demonstrated on the Mediterranean islands (Corsica and Sardinia; Barthlott and Kirshbaum, 2013) and on the alpine foothills on the northern Adriatic coastal area (Di Muzio, 2014; Davolio *et al.*, 2016). Low-level convergence upstream of the relief or over the sea is another mechanism triggering deep convection (Ducrocq *et al.*, 2008; Duffourg *et al.*, 2016).

Besides the direct orographic forcing by the elevated terrain behind the coasts and the low-level moisture convergence at sea, the formation of a low-level cold pool is another lifting mechanism susceptible to favour deep convection. Cold pools are usually generated by rainfall evaporation in subsaturated air masses around 1.5 km above sea level (asl - Ducrocq *et al.*, 2008; Bresson *et al.*, 2012). The resulting cold air parcels propagate downwards and spread to form cold pools. This cold pool, which is denser than the incoming low-level flow, acts like a relief by blocking and uplifting the moist and warm flow, resulting in a shift of the deep convection upstream. This cooling mechanism and the resulting cold pool has been demonstrated by a sensitivity study to be the main mesoscale ingredient for the quasi-stationarity of a MCS that occurred in September 2002 over the Gard plains rather than over the Massif Central foothills (Ducrocq *et al.*, 2008). Cold pools may interact or compete with orographic lifting to determine the positioning of heavy precipitation depending upon the characteristics of the incoming conditionally unstable low-level flow. Air lifting and triggering of deep convection by cold pools are especially efficient when the incoming flow is relatively dry or weak (relative humidity around 85 % and low-level wind around 15 m s⁻¹, Bresson *et al.*, 2012). Besides direct lifting of the air masses, cold pools may also deflect horizontally the incoming flow and favour or reinforce the low-level convergence (Duffourg *et al.*, 2016).

1
2
3
4 70 Better understanding these competing or interacting processes at the origin of deep
5
6 71 convection and heavy precipitation on the Mediterranean coasts in autumn is part of the objectives
7
8 72 of the HyMeX (HYdrological cycle in the Mediterranean EXperiment) programme. HyMeX is an
9
10 73 international programme dedicated to the study of the hydrological cycle and related processes in
11
12 74 the Mediterranean (Drobinski *et al.*, 2014). The first special observation period (SOP1) in autumn
13
14 75 2012 aimed at monitoring and studying these heavy precipitating events over the Mediterranean
15
16 76 coastal regions (Ducrocq *et al.*, 2014). Several Intensive Operation Periods (IOPs) focused on the
17
18 77 observation of the MCSs at the origin of these high-impact events and on investigating the
19
20 78 associated processes.
21
22
23

24 79 IOP8 on 28 September 2012 led to heavy precipitation on the Spanish Mediterranean coasts
25
26 80 (more than 200 mm (24h)⁻¹ in Andalusia, 190 mm (24h)⁻¹ in the Murcia region and 140 mm (24h)⁻¹
27
28 81 in Valencia) and was the most damaging event observed during the SOP1 (Jansà *et al.*, 2014;
29
30 82 Ducrocq *et al.*, 2016). The chronology of the event and an overview of the associated mechanisms
31
32 83 have been the subject of previous studies. Using high-resolution numerical modelling, Röhner *et al.*
33
34 84 (2016) identified orographic forcing as the main mechanism for the triggering of deep convection
35
36 85 over the coastal mountainous area, and strong low-level convergence as the mechanism at the origin
37
38 86 of deep convection at sea. Using backwards trajectories helped them to identify heat and moisture
39
40 87 local source for the conditionally unstable air masses in the Western Mediterranean basin for the last
41
42 88 and more damaging part of the event. Khodayar *et al.* (2016) evaluated the adequacy of
43
44 89 observational networks to provide information on the HPE. Describing the associated atmospheric
45
46 90 circulation and stratification at broad scale, they identified three different convergence mechanisms
47
48 91 leading to the development of deep convection over land, at the coast or at sea. These studies
49
50 92 showed that the representation of IOP8 using high-resolution numerical modelling is good, and that
51
52 93 its low-level dynamics is reasonably represented by the observations, making IOP8 a suitable case
53
54
55
56
57
58
59
60

1
2
3
4
5
6
7
8
9
10
11
12
13
14
15
16
17
18
19
20
21
22
23
24
25
26
27
28
29
30
31
32
33
34
35
36
37
38
39
40
41
42
43
44
45
46
47
48
49
50
51
52
53
54
55
56
57
58
59
60

for process study and sensitivity tests. However, they provide a rather general view of the events. In particular, none of these studies investigate in details the processes likely responsible for triggering deep convection along the coasts or on the mountainous foothills and their interplay. Especially, the presence of cold pools and their possible role in triggering deep convection are not included in the previous IOP8 studies.

Consequently, the first objective of this study is to provide a detailed analysis of the processes at the origin of the heavy precipitation that impacted the Murcia and Valencia region between 1200 UTC on 28 September 2012 and 0000 UTC on 29 September 2012. The study area and associated timing were chosen because they are susceptible to involve most of the uplifting processes described above. It constitutes a good test bed for investigating the interaction of these mechanisms initiating and maintaining deep convection on the mountainous range, over sea and on the coast. The effect of the waves generated by the wind (hereafter wind sea) on the low-level flow is usually implicitly represented in atmospheric models through the Charnock parameter and roughness length (see Eq.1 in section 3.1). As shown by a previous study on the HyMeX SOP1 IOP16a (Thévenot *et al.* 2016), a more realistic representation of the wind sea may have a significant impact on the turbulent air-sea exchanges and in the low-level flow. These authors obtained a slowing down of the low-level flow feeding the MCSs, resulting in a shift of the precipitation pattern towards sea, in better agreement with the observations. The second objective of the present study is thus to assess the impact of a better representation of the wind sea on the sea-surface roughness, momentum and heat transfer between the ocean and the atmosphere, low-level wind field and precipitation.

This paper is organized as follows. Section 2 provides an overview of the IOP8 with the synoptic context leading to the development of the HPE, the chronology of the events and a summary of the atmospheric conditions. In section 3, the numerical simulations performed on this

case study are presented together with their evaluation using satellite and field campaign observations. The outputs of the reference simulation are analysed in section 4 to provide a detailed description of the processes at the origin of deep convection and heavy precipitation on the Murcia-Valencia region. The impact of the representation of the sea state in the parameterization of the air-sea exchanges on these processes and on the precipitation is presented in section 5. Section 6 concludes with a summary of the results.

2. IOP8 overview

2.1. Synoptic context

The synoptic situation of the HyMeX IOP8 is characterized by an upper-level cut-off low over southern Portugal at 0000 UTC on 28 September 2012, progressing eastwards and reaching eastern Spain at 0000 UTC on 29 September 2012 (see Fig. 1a for the ARPEGE - Action de Recherche Petite Echelle Grande Echelle - analysis at 0000 UTC on 28 September, Fig. 1b for the synoptic analysis at 1800 UTC). The associated warm and cold surface fronts progressed northwards over the southwestern Mediterranean basin between 0600 UTC on 28 September 2012 and 0000 UTC on 29 September 2012.

2.2 Chronology of the precipitating events

The Spanish and Catalanian networks of rain gauges (MeteoCat) provide hourly observations of the precipitation amounts with a good geographical coverage (Fig. 2; see also Fig. 3b for the names of major cities and geographical locations). Heavy precipitation affected Andalusia in the morning of the 28 September between 0600 and 1200 UTC, with cumulated amount above 200 mm (Fig. 2a, 2b), then progressed eastwards to the Murcia region between 1200 and 1800 UTC (Fig. 2c, 2d) with cumulated amount of 190 mm. The Valencia region was also affected by heavy rain between 1800 and 2400 UTC on the same day (Fig. 2e, 2f).

1
2
3
4
5
6
7
8
9
10
11
12
13
14
15
16
17
18
19
20
21
22
23
24
25
26
27
28
29
30
31
32
33
34
35
36
37
38
39
40
41
42
43
44
45
46
47
48
49
50
51
52
53
54
55
56
57
58
59
60

2.3 Mesoscale convective systems and low level conditions

The multi-cell MCS responsible for the heavy rainfall on the Murcia and Valencia region originally developed around 1100 UTC over Almeria and progressed northeastwards before splitting into several systems around 1600 UTC. The near-surface wind field, as estimated by the ASCAT (Advanced SCATterometer, EUMETSAT) scatterometer onboard the Metop-A satellite between 2100 UTC on 28 September and 0000 UTC on 29 September shows three different low-level flows (Fig. 3a). North of the Mallorca island, a flow initiates in the Gulf of Lion with moderate-to-fairly-strong northerly-to-northeasterly winds converging with a slightly stronger northeasterly flow north of the Balearic Islands. This moderate low-level flow corresponds to the cold sector ahead of the warm front (hereafter ahead cold sector; Fig. 1b) and is blowing from the right side to the left side of the front. It reinforces locally to strong wind and is to some extent channeled between the Balearic Islands and the coast of Catalonia, before reaching the coasts of the Valencia region. South of Ibiza and between North Africa and the coasts of southeastern Spain, a southwesterly moderate flow characterizes the cold sector behind the cold front (hereafter rear cold sector). Between these two regions, the warm sector is characterized by a light-to-moderate easterly-to-northeasterly low-level flow. This low-level flow distribution results in a strong surface convergence line located along the warm front between the warm and moist easterly flow on the warm sector and the rapid southwesterly flow between southern Spain and North Africa. In the following, we focus on the Murcia-Valencia region and we investigate the processes at the origin of deep convection (especially the possible role of cold pools) using the modelling tools that are presented in the next part.

3. Meso-NH simulations

3.1. Meso-NH model and set-up

The numerical simulations were performed with the non hydrostatic numerical research model Meso-NH (Lafore *et al.*, 1998). The Meso-NH model was run over a $1125 \times 1125 \text{ km}^2$ domain covering the western Mediterranean basin from Gibraltar to the west of Sardinia (Fig. 3b). It encompasses the precipitating systems during their whole life-cycle as well as the different marine low-level moisture-supplying flows. The horizontal grid has a 2.5-km resolution, and the vertical grid is defined with 55 stretched vertical levels (Gal-Chen and Somerville, 1975) up to 20 km, with 18 levels in the lowest 1500 m above the surface. The model resolution and associated physical parameterization package are the same as those used in previous studies of HPEs using Meso-NH (e.g. Nuissier *et al.*, 2008, Thévenot *et al.*, 2016, Duffourg *et al.*, 2016).

The prognostic variables of the model are the three components of the wind, the dry potential temperature, the turbulent kinetic energy and the mixing ratios of the water vapour and of five different classes of hydrometeors (cloudwater, rainwater, primary ice, snow aggregates, and graupel). The evolution of the water species are governed by a bulk microphysical scheme (Caniaux *et al.*, 1994; Pinty and Jabouille, 1998). The parameterization of the turbulence is based on a 1.5-order closure (Cuxart *et al.*, 2000) with the diagnostic mixing length option following Bougeault and Lacarrère (1989). Thanks to its high horizontal resolution, the atmospheric deep convection is explicitly solved by the model. The surface conditions and the air–surface exchanges are governed by the SURFEX surface model (Masson *et al.*, 2013). The sea-surface turbulent fluxes are parameterized using the COARE 3.0 formula (Fairall *et al.*, 2003). The sea-surface roughness is related to the friction velocity u_* using the Charnock coefficient α_{ch} :

$$z_0 = \alpha_{ch} \frac{u_*^2}{g} + 0.11 \frac{\nu}{u_*} \quad (1),$$

where g is the gravitational acceleration and ν the kinematic viscosity.

Simulations start on 28 September 2012 at 0000 UTC and last 24 h. They are initialised and driven at their lateral boundaries every 3 h from the high-resolution AROME-WMED analyses (Application of Research to Operations at Mesoscale – Western Mediterranean; Fourrié *et al.*, 2015). The sea-surface temperature (SST) field comes from the initial AROME-WMED analysis, which is built with the 2D Optimal Interpolation of *in situ* measurements CANARI (Code d'Analyse Nécessaire à Arpege pour ses Rejets et son Initialisation; Taillefer, 2002) blended with the Operational Sea Surface Temperature Ice Analysis (OSTIA; Donlon *et al.*, 2012). This SST field remains constant during the 24-h integration.

3.2 Sensitivity to sea state representation

In order to test the sensitivity of the boundary-layer processes and of the HPEs to the sea state, two simulations were performed with and without explicitly representing the wave impact into the surface turbulent fluxes parameterization. The methodology used here follows closely the one used by Thévenot *et al.* (2016) with the use of the sea state analyses taken from the run of the Wavewatch III® wave model (Ardhuin *et al.*, 2010; Tolman, 2014) in the Previmer project framework (<http://www.previmer.org>) as a surface forcing of the Meso-NH/SURFEX model.

In the experiment with no wave impact (NOWAV hereafter, used throughout this study as a reference simulation), the COARE 3.0 algorithm is used with the formulation of the Charnock coefficient from Hare *et al.* (1999), *i.e.* α_{ch} is set to 0.011 for 10-m wind speed below 10 m s^{-1} , then increases linearly up to 0.018 at 18 m s^{-1} , and remains constant for larger wind speeds. In the experiment with explicit wave representation (WW3_F hereafter), the formulation of Oost *et al.*

(2002) is used with the wave peak period provided by the analysis every 3 h:

$$\alpha_{ch} = 50 (c_p / u_*)^{-2.5} \quad (2),$$

where c_p is the wave phase velocity. The Wavewatch III® wave parameters have been compared with two Météo-France buoy observations in the Gulf of Lion and Azur sites. Mean biases are of 0.16 and 0.36 m for the significant wave height (root mean square 0.25 m) and of 1.0 and 0.9 s for the peak period (root mean square 0.6 and 0.5 s), respectively. This level of agreement is comparable to what has been obtained in a previous study (Thévenot *et al.*, 2016) and makes us confident in using these analysed parameters as a forcing representative of the actual sea state over the western Mediterranean basin.

4 Validation of the reference simulation

The results of the NOWAV reference simulation were compared to observations in order to assess the skill of the simulation in representing the processes and the chronology of the events. All the observations used in this work were collected and have been made available in the HyMeX project framework.

4.1 Precipitation

The observations used in this part are taken from the Spanish rain gauge network including the dense network of METEOCAT. The amount and location of the precipitation simulated in NOWAV display a good match with the rain gauge 3-h cumulative precipitation from 0600 UTC on 28 September 2012 to 0000 UTC on 29 September 2012 (Fig. 2a to 2f). The maximum cumulative amount observed by the rain gauges available for this study is 204 mm (24h)⁻¹ over the whole domain, that compares favourably with the maximum predicted by the NOWAV simulation of 212 mm (24h)⁻¹. To assess more precisely the skill of our two simulations, scores against rain gauge

1
2
3
4
5
6
7
8
9
10
11
12
13
14
15
16
17
18
19
20
21
22
23
24
25
26
27
28
29
30
31
32
33
34
35
36
37
38
39
40
41
42
43
44
45
46
47
48
49
50
51
52
53
54
55
56
57
58
59
60

observations for the 24-h period starting at 0000 UTC on 28 September over the whole simulation domain have been computed. The simulated daily rainfall amounts are extracted at the closest grid point to the 1233 rain gauge stations. The mean bias, the standard deviation of the difference (SDD), and the correlation coefficient (r) are given in Table 1, as well as two categorical scores widely used for assessing skills of precipitation forecast: the Equitable Threat Score (ETS; Schaefer, 1990) and the Hanssen and Kuipers discriminant (HK; Hanssen and Kuipers, 1965). Both scores assess the ability of the model to detect rainfall amounts above a given threshold (see Table 1) and give values between -1 and 1. The thresholds used here correspond roughly to the 4-, 5- and 6-quantiles in the observations. ETS excludes the probability of detecting an event by chance, values equal to (resp. below) zero indicates that model skills are equal to (resp. below) a random forecast. HK measures the accuracy of the forecast both for events and non events, HK=0 corresponds to a constant forecast and HK=-1 to zero hits both for events and non-events forecasts.

The scores obtained here are high, showing that the representation of this event by our two simulations is much better than random or constant forecast and performs very well in predicting both events and non events.

4.2 Low-level flow and stability

The wind field at the first vertical level of the model over sea is compared with the wind field obtained from the ASCAT scatterometer onboard Metop-A (Fig. 3) and shows a good agreement in intensity and direction. Especially, the near-surface convergence line corresponding to the front between Ibiza and Mallorca is well represented in the simulation, as well as the lower intensity of the low-level wind in the warm sector area. Here and in the rest of the study the cold and warm fronts are determined using the 2-m temperature gradients. The occluded front is determined using the low-level wind convergence.

1
2
3
4 251 The radiosoundings performed in Palma de Mallorca and Barcelona on 28 September at
5
6 252 1800 UTC and on 29 September at 0000 UTC are used to assess the skills of the NOWAV
7
8 253 simulation in reproducing the wind field at different levels and the air masses stability profiles from
9
10 254 the equivalent potential temperature (θ_e , Fig. 4). These radiosoundings were assimilated in the
11
12 255 AROME-WMED analyses used as large-scale forcing of our simulations (Fourrié *et al.*, 2015).
13
14
15 256 Their impact on the NOWAV simulation is probably weak, since they occur late in the simulation
16
17 257 and far from the domain boundaries. Observed and simulated radiosounding profiles generally
18
19 258 agree well on the θ_e and wind values. In Barcelona, the simulated wind speed is systematically
20
21 259 lower than in observations especially at upper level, though the agreement on the direction is very
22
23 260 good. In particular, the veering of the wind at 1800 UTC from east-north-east at the surface to south
24
25 261 at 5000 m asl and south-west at upper level that can be observed on the two stations is well
26
27 262 reproduced by the simulation. The tropopause height is close to 12 km at both locations and times.
28
29
30

31 263 At 1800 UTC, the Palma sounding is still located in the cold sector ahead of the incoming
32
33 264 warm front (Fig. 4a). The ground equivalent potential temperature is 50-55°C in the simulation,
34
35 265 increasing up to 60°C at 1000 m asl, then decreasing to 50°C at 3000 m asl. The low-level wind is
36
37 266 northeasterly, close to 12 m s⁻¹, weakening to 5 m s⁻¹ at 2000 m asl. At 0000 UTC on 29 September
38
39 267 (Fig. 4b) Palma is now in the warm sector as shown by the increase of the surface θ_e up to 55-65 °C
40
41 268 in the simulation. The simulated potential temperature at low level is generally higher than in
42
43 269 observations though their profiles up to 3000 m asl are very similar. This warm and moist low-level
44
45 270 layer goes up to 2000 m asl with some instability remaining up to 4000 m asl in the simulated
46
47 271 profile. The low-level wind is weak (up to 4000 m asl) in the warm sector, as already noticed
48
49 272 (section 2.3 and Fig. 3).
50
51
52
53

54 273 The two Barcelona profiles exhibit a similar evolution between 1800 UTC and 0000 UTC
55
56 274 (Fig. 4c and d), with equivalent potential temperatures close to 40°C at the surface. Barcelona
57
58
59
60

1
2
3
4
5
6
7
8
9
10
11
12
13
14
15
16
17
18
19
20
21
22
23
24
25
26
27
28
29
30
31
32
33
34
35
36
37
38
39
40
41
42
43
44
45
46
47
48
49
50
51
52
53
54
55
56
57
58
59
60

profiles are in the ahead cold sector at both time periods, with the occluded front approaching from the south on 29 September at 0000 UTC. At both times the wind is weak from east close to the ground, about 15 m s^{-1} at 1000 m asl, and from south to southeast at upper level. At 1800 UTC, the low- θ_e air masses close to the ground transported from the sea by the northeasterly low-level flow are topped by a thick layer of warmer, stable air (θ_e close to 55°C) from 700 to 3000 m asl. At 0000 UTC on 29 September, the low- θ_e layer below 700 m asl is still present with a sharper vertical gradient (likely maintained by the low-level cold and moist easterly flow) but the warmer air layer located just above is now thinner with θ_e close to 50°C up from 2000 m asl. This can be explained by a strong and homogeneous flow observed in the simulation outputs between 2000 and 4800 m asl transporting drier air with θ_e below 48°C from the south of the western Mediterranean basin (not shown).

In summary, the reference simulation succeeds in reproducing the stability (θ_e) variations observed in the radiosoundings. The profiles of wind direction and wind speed at first order is also well reproduced by the model (except in Barcelona for the wind speed). We consider in the following that this simulation can be confidently used to investigate the fine-scale processes leading to deep convection and heavy precipitation in the Murcia-Valencia region.

5. Process study

In this part, the reference simulation outputs are used to study the different processes at play on the eastern Spanish coast between Murcia and Valencia between the 28 September 2012, 1600 UTC (corresponding to the start of convective precipitation in the Murcia region) and the 29 September 2012, 0000 UTC.

5.1 Conditional instability, moisture convergence and low-level jet

As seen in the previous part, the low-level flow over the western Mediterranean on the afternoon of

the 28 September is organized in three main areas: the ahead cold sector on the Balearic Sea and the Gulf of Lion; the warm sector from the Balearic Islands to Murcia and the coasts of North Africa; and the rear cold sector on the Alboran Sea up to Murcia. This organization is well reproduced by the NOWAV simulation with a strong low-level convergence line (Fig. 5a) along the surface cold and occluded fronts. The equivalent potential temperature at the first level of the model (Fig. 5b) shows value above 64°C in the warm sector with maximum values above 70°C on a large area north of the Algerian coasts. This warm sector is limited by very sharp θ_e gradients: to the south by a low-level rather uniform southerly flow bringing warm and much drier air from the African continent and to the southwest by the cold front with the rear cold sector with equivalent potential temperature below 58°C. On its north edge, the θ_e gradient corresponding to the warm front is much smoother. However, θ_e decrease to 54°C on a large area of the Gulf of Lion and the northern Balearic Sea. Over Spain θ_e is lower, confirming that there is no local feeding or development of convective systems on land away from the coasts (Röhner *et al.*, 2016). The Convective Available Potential Energy (CAPE) at the same time (Fig. 5c) shows values above 1000 J kg⁻¹ and up to more than 2000 J kg⁻¹ on a large area within the warm sector, ahead of the low-level flow close to the cold front. This high-CAPE area is limited to the north by the ahead cold sector and to the south by the low-level still warm but much drier southerly flow from North Africa. Its southwestern boundary corresponds to the cold front off Murcia at that time, where strong moisture convergence occurs. The Convective Inhibition (CIN, Fig. 5d) is relatively high in the main part of the warm sector, especially north of the North African coast due to the warm and dry southerly flow. By contrast, it shows low values in the westernmost part of the warm sector in the lee of the warm and moist flow. This area at the southwestern edge of the warm sector – with high CAPE and low CIN values – is thus the area the most prone to feed deep convection processes.

The simulated radar reflectivities show values above 40 dBz corresponding to convective

1
2
3
4
5
6
7
8
9
10
11
12
13
14
15
16
17
18
19
20
21
22
23
24
25
26
27
28
29
30
31
32
33
34
35
36
37
38
39
40
41
42
43
44
45
46
47
48
49
50
51
52
53
54
55
56
57
58
59
60

precipitation at two different places (Fig. 5b to d, green contour): along the occluded front the low-level moisture convergence above $3 \times 10^{-5} \text{ kg m}^{-3} \text{ s}^{-1}$ (Fig. 5a, green contour); and on land close to Murcia, probably as a result of stationarity of a previous convective system. At sea, the mechanism responsible for the convective precipitation is clearly the strong low-level convergence that remains present along the occluded front and on the triple point between 1500 UTC on 28 September and 0000 UTC on 29 September.

In the ahead cold sector, the 10-m northeasterly wind of $12 \text{ to } 15 \text{ m s}^{-1}$ reinforces to $16 \text{ to } 20 \text{ m s}^{-1}$ at 500 m asl (Fig. 5a, 6a). At 1500 m asl, by contrast, the NOWAV simulated wind field is a more uniform southeasterly flow around 12 m s^{-1} on the ahead cold sector and part of the warm sector (Fig. 6b). The ahead cold sector flow corresponds therefore to a strong low-level jet (LLJ). Note that this LLJ is clearly visible in the observed and simulated radiosounding profiles in Palma de Mallorca at 1800 UTC and in Barcelona at 1800 UTC and at 0000 UTC (Fig. 4). Oppositely to what has been frequently observed in HPE studies (e.g. Ducrocq et al., 2008), this LLJ is not located in the warm sector corresponding to the conditionally unstable feeding of the convective systems but in a cold sector with θ_e at low level between $48 \text{ and } 60^\circ\text{C}$. It corresponds likely to a low-level jet associated with the low-level pressure gradient ahead of the warm front (e.g. Shapiro and Keyser, 1990).

This low-level flow is not saturated in humidity as shown by the surface latent heat flux values up to 500 W m^{-2} on a large area at 1600 UTC on 28 September (Fig. 7a - corresponding relative humidity values between 70 and 80 %). The ahead cold sector is the only place in the western basin where such values are observed at that time (except very locally under the convective systems, probably in link with wind gusts). This is due to the conjunction of this strong LLJ with dry air masses over the Gulf of Lion and with SST above 23°C all over the Balearic Sea as seen in the OSTIA analysis (not shown). By contrast, the SST in the Gulf of Lion is much colder ($18 \text{ to } 20^\circ\text{C}$).

20°C) due to an episode of Mistral-Tramontane in the previous days; this results in weak evaporation. As a result of this very strong evaporation on the Balearic Sea, the mixing ratio in the LLJ ranges between 8 and 10 g kg⁻¹ over the main evaporative patch (Fig. 7b). It increases gradually when approaching the eastern Spanish coasts, up to 13 g kg⁻¹ (see also Fig. S1 and S2 in the Supporting Information). This rising of humidity from 8 g kg⁻¹ to more than 12 g kg⁻¹ was already seen along backward trajectories in the study of Röhner *et al.* (2016). These air masses coming from the Gulf of Lion have potential temperatures between 18 and 20°C. They warm up slightly over the northern Balearic Sea thanks to the strong turbulent heat transfer and approach the Spanish coasts with potential temperature close to 23°C (see Fig. S1 and S2).

Cold and relatively dry air masses originating from the Gulf of Lion are transported by the LLJ to the Spanish coasts close to Valencia. They moisten and get slightly warmer due to turbulent exchanges with a warmer sea over the Balearic Sea.

5.2 Initiation and maintenance processes

We now investigate in more details the processes responsible for the initiation and maintenance of the deep convection in the Murcia-Valencia region, between 1600 and 2300 UTC on 28 September. At this time period, various processes leading to heavy precipitation interact and compete with each other.

The virtual potential temperature (θ_v) is directly related to the density of air masses and commonly used as a proxy for cold pools (e. g. Ducrocq *et al.*, 2008; Bresson *et al.*, 2012). In the following, we use θ_v values under 23°C to identify cold pools, in addition to θ_e characterizing the heat and moisture content of the inflow.

At 1600 UTC, low values of θ_v are associated with the LLJ in the western part of the Balearic Sea. They correspond to the cold and moist air masses transported from the Gulf of Lion by the

1
2
3
4
5
6
7
8
9
10
11
12
13
14
15
16
17
18
19
20
21
22
23
24
25
26
27
28
29
30
31
32
33
34
35
36
37
38
39
40
41
42
43
44
45
46
47
48
49
50
51
52
53
54
55
56
57
58
59
60

LLJ, as previously described. These air masses are sufficiently cold to make them dense in spite of their moisture and they accumulate on the foothills of the relief at the latitude of Valencia (Fig. 8a). The role of this LLJ in initiation of the cold pool on the coast is confirmed on the vertical cross section along this LLJ (Fig. 8c). Dense air masses with low θ_v are present up to 600 m asl and transported by this 15-to-18 m s⁻¹ flow towards the coast. Convective precipitation with instantaneous rates above 20 mm h⁻¹ are present southwest of Xabia on land and offshore (Fig. 8b). They correspond to strong vertical velocities at 500 m above ground level (agl) (Fig. 8a, white contour) and moisture convergence rates above 3 10⁻⁵ kg m⁻³ s⁻¹ at the surface (Fig. 8b, blue contour). Strong convergence at sea is thus the mechanism initiating the convection at that time, with both the LLJ in the ahead cold sector and the weaker flow in the warm sector contributing to the moisture feeding. South of Valencia, along the 2D profile (Fig. 8c) strong convective precipitation correspond to strong vertical velocities (white and black contours) and are located close to the maximum of the topography. The horizontal convergence on the relief slope (vertical blue arrows, Fig. 8c) is the mechanism responsible for the uplift and the corresponding deep convection at that place and time.

At 1830 UTC (Fig. 9), the warm and cold fronts bounding the conditionally unstable air mass have moved northeastwards. On the southernmost part of the area, the limit of the convective precipitation with instantaneous rates above 20 mm h⁻¹ matches exactly the northern edge of the cold pool (north of Murcia) which is also accurately collocated with strong uplift (Fig. 9a, white contour) and strong moisture convergence rates (Fig. 9b, blue contour). At sea, convective precipitation patches are located on the cold and occluded fronts, and corresponds also to strong convergence rates (Fig. 9b, blue contour). Along the coasts south of Valencia, very high instantaneous rain rates (50 mm h⁻¹) are obtained over the sea not associated with high convergence rates (Fig. 9b, 9c). However, their contour (see the instantaneous rates above 20 mm h⁻¹ on Fig. 9b)

393 matches the cold pool present along the coast at the latitude of Valencia, which is the result of both
394 moisture feeding by the northeast LLJ and rain evaporation. Vertical cross sections exhibit two
395 different mechanisms contributing to initiating the deep convection by uplift of the air masses. On
396 the relief as precedently, strong uplift with vertical velocities above 5 m s^{-1} is obtained, resulting in
397 instantaneous rain rate of 50 mm h^{-1} . Over the sea, close to the edge of the cold pool which has
398 developed since 1600 UTC, vertical velocities above 1 m s^{-1} above 1500 m agl (white contour, Fig.
399 9c) result in deep convection. The horizontal convergence (blue vertical arrows, Fig. 9c) is strong at
400 the edge of the cold pool. As no convective cells are present at that place yet, the cold pool is very
401 likely at the origin of the uplift here. On the cold pool itself, strong uplift (white contour) and strong
402 convergence (blue arrows) are collocated with downdraughts with θ_e below 52°C and subsidence
403 below -1 m s^{-1} (black contour), and strong precipitation. At this place, the active convective cells
404 and strong precipitation seem to maintain (and enhance) the cold pool.

405 At 2000 UTC, the main convergence zone along the occluded front is now located south of
406 Valencia (Fig. 10a). The two areas of strong convective precipitation are still present on the relief,
407 northwest of Xabia and south of Valencia. They are collocated with strong convergence rates (Fig.
408 10a, white contour; Fig. 10b, blue contour) and high evaporation at low level on the relief and on
409 the cold pool (not shown). Conversely, at sea off Valencia, strong precipitation rates are not
410 collocated with strong moisture convergence (Fig. 10b), they rather correspond to the coldest patch
411 of the cold pool at sea (Fig. 10a). The surface covered by the cold pool over the sea has slightly
412 increased and the minimum θ_v on land has decreased down to 17°C . Strong uplifts (white contour,
413 Fig. 10c) collocated with strong horizontal convergence (blue arrows, Fig. 10c) and strong
414 precipitation (Fig. 10b) are located at the edge of the cold pool. Convergence and uplift at the edge
415 of the cold pool are the processes resulting in deep convection here. The already active convection
416 on the relief generates downdraughts (black contour, Fig. 10c) that in turn contribute to the

1
2
3
4
5
6
7
8
9
10
11
12
13
14
15
16
17
18
19
20
21
22
23
24
25
26
27
28
29
30
31
32
33
34
35
36
37
38
39
40
41
42
43
44
45
46
47
48
49
50
51
52
53
54
55
56
57
58
59
60

417 maintenance of this cold pool on the relief foothills and at sea. On these cold pools at the latitude of
418 Valencia, a deflection of the low-level wind from east-north-east to north-north-east corresponds to
419 the initiation of a barrier wind (Fig. 10a, insert). Barrier winds have been observed and modelled in
420 previous studies, mostly around the Adriatic Sea (Di Muzio, 2014, Davolio *et al.*, 2016). The
421 altitude of the mountainous area around Valencia makes it comparable to what is obtained by Di
422 Muzio (2014) with a medium-height orography.

423 At 2130 UTC, the surface covered by the cold pools has further extended at sea, in particular
424 off Xabia (Fig. 11a) and the main moisture convergence zone has reached the latitude of Valencia
425 (Fig. 11b, blue contour, Fig. 11c). The very strong convergence zone offshore is still present with
426 high precipitation rates (see Fig. 11c, blue arrows) in collocation with modelled uplift and
427 downdraughts. On the relief at the latitude of Valencia, high precipitation rates are also collocated
428 with the strong convergence line that progresses northwards with the precipitation patterns.
429 Between these two areas, large patches of very strong precipitation (instantaneous rain rate up to
430 130 mm h^{-1} , Fig. 11c) are obtained along the coast, at the latitude of Valencia, in very good
431 collocation with the cold pool extending at sea. Clearly, low-level convergence (blue arrows Fig.
432 11c) is the mechanism responsible for the uplift triggering the deep convection here. It is however
433 difficult to attribute this convergence to the cold pools effect only, as convective cells are already
434 present here. A secondary cyclonic circulation has formed at low level (Fig. 11a, insert), due to the
435 deflection of the low-level wind by the cold-pool edge. It results in shifting the eastern edge of the
436 cold pool southeastwards, and the patches of strong moisture convergence northwards (Fig. 11b).
437 This low-level secondary circulation has already been observed on HPEs (Berthou *et al.*, 2016;
438 Duffourg *et al.*, 2016) as a result of a barrier wind formation. It corresponds here to the minimum of
439 sea-level pressure (see Fig. 12a) and results in a slight bending of the convergence zone at sea. In
440 order to check whether these instantaneous high rain-rates at sea are also present in the

observations, the radar reflectivities obtained in the NOWAV simulation at 2100 UTC are compared with the corresponding observations from the OPERA radar reflectivity Odyssey composite (Fig. 13; the Odyssey product is not available at 2130 UTC; <http://www.knmi.nl/opera/>). The rain amounts are comparable between observations and simulation outputs, and the bending of the convection patterns due to the cold pool and associated to the secondary cyclonic circulation in the NOWAV simulation is also present in the observations.

The mechanisms at the origin of heavy precipitation in the Murcia-Valencia region involve orographic forcing on the coastal mountainous range, very strong moisture low-level convergence at sea along the cold front and lifting of the moist LLJ by cold pools that developed on the relief foothills and propagated offshore. These cold pools induce a northerly-to-northwesterly weak barrier wind along the coast, and the setup of a low-level secondary cyclonic circulation resulting in the bending of the convective patterns. These processes play a key role in the location and distribution of heavy precipitation (rainfall cumulative amount above 140 mm in 6 hours) in the Valencia region. In particular, they explain the rainfall patterns at sea as observed in the radar reflectivity images (Fig. 13).

6. Impact of wave representation

In this part, we discuss the impact of representing explicitly the waves in the WW3_F simulation through the forcing of the Meso-NH model at the surface using the 3-h Wavewatch III® analyses. The objective here is to test the sensitivity of the atmospheric response to the representation of the surface roughness. As shown by Thévenot *et al.* (2016) on another HPE case study, representing the surface roughness variability due to the wind sea can result in a slowing down of the low-level wind and in a shift of the precipitation place. As shown by the scores of the WW3_F simulation, which are not significantly different from those of NOWAV (Table 1), the overall representation of the

1
2
3
4
5
6
7
8
9
10
11
12
13
14
15
16
17
18
19
20
21
22
23
24
25
26
27
28
29
30
31
32
33
34
35
36
37
38
39
40
41
42
43
44
45
46
47
48
49
50
51
52
53
54
55
56
57
58
59
60

high precipitation is comparable in both simulations.

6.1 Instantaneous effect on the low-level flow

We first examine the wave parameters as simulated by the Wavewatch III® model at 1500 UTC on 28 September, and their instantaneous impact on the oceanic and atmospheric surface parameters. The simulated significant wave heights are the largest (more than 2.5 m) on the Balearic Sea and south of the Balearic Islands along the coasts of Spain, between Murcia and Xabia (Fig. 14a). The resulting surface roughness difference as parameterized in COARE 3.0 depends mainly on the 10-m wind speed at sea and on the state of development of the wind sea (represented by the significant wave height). This difference is then the biggest in the ahead cold sector, where both strong winds at 10 m (Fig. 5a) and waves in equilibrium with the wind (Fig. 14a) are present. Roughness length differences are above $5 \cdot 10^{-4}$ m over a large area (Fig. 14b), which result in a difference on the drag coefficient C_d of $0.2 \cdot 10^{-3}$ over the whole ahead cold sector (Fig. 14c). Local strong increase of the roughness length (up to $8 \cdot 10^{-3}$ m) and of the drag coefficient is also observed more locally under the convective systems and in the rear cold sector. These general increases over the ahead cold sector result in a slowing down of the 10-m wind of more than 0.5 m s^{-1} over a very large area of the ahead cold sector (Fig. 14d). The part of the rear cold sector close to the front shows slowing down of the same magnitude and local patches of wind slowing down by more than 5 m s^{-1} are also observed under the convective systems, collocated with the surface roughness increase. These patches concern very limited areas and are collocated with strong wind and gusts under the convective clouds.

This instantaneous impact of the waves on the low-level flow is different from what has been obtained on another case study (IOP16a) using the same methodology (Thévenot *et al.*, 2016) by two aspects. Firstly, the wind slowing down is weaker than what was obtained by these authors

in average (0.5 m s^{-1} to be compared to 3 m s^{-1}), but concerns a larger area. Secondly, this slowing down concerns the two cold sectors, especially the ahead cold sector that contribute to the cold pool initiation and maintenance, but does not impact the warm sector and the feeding of the convective systems by conditionally unstable air masses.

In atmospheric and oceanic surface conditions corresponding to HPEs, the turbulent heat transfer over the sea is generally dominated by the latent heat flux. This is the case here, with strong evaporative fluxes in a large area of the ahead cold sector (see Fig. 7a) between 1500 and 1900 UTC, as well as locally in the rear cold sector. The differences on the latent heat flux due to the wave representation in the surface forcing of the model are however very weak: 5 W m^{-2} increase on average with mean values of the latent heat flux close to 200 W m^{-2} in the two cold sectors of this simulation. The effect on the low-level air masses participating in the feeding of the systems (θ_e , mixing ratio) is consequently not significant. As in the study of Thévenot *et al.* (2016), the mechanisms responsible for a possible change in the deep convection and associated heavy precipitation are to be found more likely in dynamical effects of the low-level flow than in the thermal exchanges.

6.2 Impact on the precipitation field

We now compare the equivalent and virtual potential temperature fields at the first level of the model, at 2130 UTC in the region of Murcia-Valencia, in order to investigate the impact of the wave representation on the convective systems and precipitation. Few differences are observed in the low-level flow feeding the systems itself (Fig. 12; see also Fig. S3 in Supporting Information). The main differences concern the cold pools that extend further east at sea in the WW3_F simulation, especially at the latitude of Valencia. They also show colder θ_v on the coast north of Valencia. As a consequence of this cold pool shift, the precipitation field above 5 mm h^{-1} (instantaneous rain rate;

1
2
3
4
5
6
7
8
9
10
11
12
13
14
15
16
17
18
19
20
21
22
23
24
25
26
27
28
29
30
31
32
33
34
35
36
37
38
39
40
41
42
43
44
45
46
47
48
49
50
51
52
53
54
55
56
57
58
59
60

see yellow contour in Fig. S3) is displaced eastwards. In every simulation, the patterns corresponding to 5 mm h⁻¹ rain rate closely follow the edge of the cold pools (corresponding to θ_v under 23°C). This is due to the displacement of the moisture convergence line at the surface on the edge of the cold pool (Fig. 12).

The secondary cyclonic circulation at the eastern edge of the cold pool, which is observed at 2130 UTC in the NOWAV simulation (section 5.2, Fig. 11a and 12a), is weakened and displaced at sea in the WW3_F simulation (Fig. 12b). In both simulation outputs, the 10-m wind field is deflected and bended by the cold pool edge, resulting in the WW3_F simulation in a shift of this cyclonic circulation 30 km eastwards. The sea-level pressure field at 2130 UTC on 28 September 2012 in the reference simulation NOWAV shows two minima close to 1000 hPa at the latitude of Valencia, corresponding to the well-organized secondary low-level circulation (Fig. 12a). In the WW3_F simulation, higher sea-level pressures up to 1012 hPa are observed near the coast, and the sea-level pressure minimum of 1001 hPa is displaced 30 km towards Ibiza, out of the cold pool (Fig. 12b). This weakening of the local sea-level pressure minimum has been observed in previous sensitivity studies and can be explained by the slowing down of the low-level wind in WW3_F. Relative higher pressures result, in turn, in an anticyclonic shift of the surface wind and of the displacement of the cyclonic circulation towards sea (Berthou *et al.*, 2016). A weak barrier wind effect is also observed on the cold pools in both simulation.

As a result, the precipitation cumulated over 6 h from 1800 UTC on 28 September to 0000 UTC on 29 September 2012 show a significant difference in both their amount and their location between WW3_F and NOWAV (Fig. 15). Taking into account the wave effect on the surface roughness results in rain amount more distributed along an east-west profile (Fig. 15b). The peak of precipitation on this 6-h time period over the whole simulation domain reaches 159 mm in the WW3_F simulation with respect to 258 mm in the NOWAV simulation. The total amount on the

Valencia area is the same in both simulations with an average of 2.05 mm km^{-2} . As seen in Figure 15a, the precipitation pattern in the WW3_F simulation results is displaced of 50 km towards sea. Note however that this displacement concern precipitation located mainly at sea and does not affect the forecast scores (Table 1) since they were computed using raingauges observations.

This impact of a weakening of the low-level wind field of less than 1 m s^{-1} due to wave representation on the formation and maintenance of cold pools in the coastal domain can be explained by the results of previous studies. Cold pools are known to develop more easily and over larger areas with slower low-level winds (Bresson *et al.*, 2012; Davolio *et al.*, 2016). Lower wind speeds results in more time for the convective cells to develop and for the cold pools to strengthen themselves from evaporating precipitation (Bresson *et al.*, 2012). This relatively low but uniform weakening of the low-level wind induces a significant change on the cold pool extent and location, resulting in a corresponding displacement of the heavy precipitation patterns.

7. Summary and conclusion

This study is part of the HyMeX programme, the objectives of which include a better understanding of the mechanisms triggering the deep convection responsible for heavy precipitation, and the role of the air-sea exchanges in the case of Mediterranean HPEs. In the framework of this programme, the SOP1 IOP8 has been the subject of several studies, either using high-resolution simulations for describing the main mechanisms responsible for deep convection (Röhner *et al.*, 2016), or using observations for a general description of the event (Khodayar *et al.*, 2016). These authors do not provide a detailed study neither of the different mechanisms responsible for uplifting the air masses in a coastal area, leading to strong precipitation, nor of the role of the sea surface exchanges in the event.

Here, we focused on the local processes leading to heavy precipitation in the Murcia-

1
2
3
4
5
6
7
8
9
10
11
12
13
14
15
16
17
18
19
20
21
22
23
24
25
26
27
28
29
30
31
32
33
34
35
36
37
38
39
40
41
42
43
44
45
46
47
48
49
50
51
52
53
54
55
56
57
58
59
60

Valencia region between 1600 and 2300 UTC on the 28 September 2012, on their interaction, and on the role of the sea state representation in a model. The use of the non-hydrostatic, convection-permitting model Meso-NH without and with a more realistic representation of the sea surface roughness provides very accurate representation of the low-level flows and atmospheric stability patterns. In particular, the precipitation amounts, distribution and chronology from 1200 UTC on 28 September to 0000 UTC on 29 September are well reproduced by both simulations. The precipitation scores of the reference simulation computed with different thresholds give also excellent results. We then consider these reference simulation outputs suitable for investigating the mechanisms at the origin of this HPE with maximum cumulative rain amount above 200 mm in 24 h.

Several mechanisms represented in the simulation outputs have been described in previous studies on the same HPE (Röhner *et al.*, 2016; Khodayar *et al.*, 2016). For instance, the warm and cold sector associated play a role in the moisture and heat feeding of the system when it moves northwards along the Mediterranean Spanish coast from Gibraltar to Catalonia. Low-level conditionally unstable air masses with very high CAPE and low CIN reach eastern Spain in a easterly weak-to-moderate flow. The two main mechanisms mentioned in previous studies, responsible for the lifting of these air masses and leading to the triggering of the deep convection - namely orographic forcing on land and strong low-level moisture convergence at sea - were assessed in our reference simulation. The present study reveals other mechanisms at the origin of the deep convection and heavy precipitation (see Fig. 16 for a synthetic scheme). The LLJ is observed here in the ahead cold sector rather than in the main warm low-level fuelling the MCS. It originates in the Gulf of Lion and transports very cold air masses, which barely warm up over the warmer surface waters of the Balearic Sea. These cold thus dense air masses contribute to initiate cold pools on the relief foothills close to the sea. Rain evaporation in the subsaturated mid-level

layer results in downdraughts further developing and maintaining these cold pools. They eventually act as triggering mechanisms of the deep convection when the air masses at their leading edge are thick and dense enough to uplift the incoming conditionally unstable air masses. A weak barrier wind develops from 2000 UTC on 28 September at low level over the cold pool at sea, leading to a cyclonic deflection of the incoming low-level flow (Fig. 11a). A secondary cyclonic circulation results in a bending of the cold pool edge, and in a deflection of the strong low-level convergence zones at sea and of the corresponding convective precipitation. Cold pools play here a key role in the localization of the deep convection and associated heavy precipitation at sea off Valencia rather than on the relief foothills.

Representing in a more realistic way the sea state using the 3-hourly Wavewatch III® analyses as a forcing has a significant impact on the simulation results. It first increases the surface roughness, resulting in an increase of the wind stress, thus in a slight decrease of the low-level wind. The main conditionally unstable low-level flow feeding the convective systems in warm and moist air is not impacted, but the moderate wind slowing down over a large part of the secondary flow in the ahead cold sector (low-level jet) is sufficient to affect significantly the location of the heavy precipitation at sea in the Valencia region. The cold pools are displaced further at sea, strengthened, and shift accordingly the place of strong convergence and convective precipitation. The sea-level pressure field is changed towards higher pressures and the low-level wind field is modified accordingly by an anticyclonic shift.

Conversely, no impact of the wind sea on the heat exchanges at the sea surface has been observed in this study. The mean change of the latent heat flux of 5 W m^{-2} over the Balearic Sea does not change significantly the moisture content or equivalent potential temperature in the LLJ feeding the convective systems. This reinforces the similar results obtained in a previous study on the HyMeX SOP1 IOP16a (Thévenot *et al.*, 2016). Either developed wind sea concerns the area of

1
2
3
4
5
6
7
8
9
10
11
12
13
14
15
16
17
18
19
20
21
22
23
24
25
26
27
28
29
30
31
32
33
34
35
36
37
38
39
40
41
42
43
44
45
46
47
48
49
50
51
52
53
54
55
56
57
58
59
60

warm and moist air directly feeding the HPE, as this was the case in IOP16a, and the low-level flow is already saturated in humidity; as a result, the latent heat transfer change due to waves is weak. Or it concerns an area not saturated in humidity yet as this is the case in IOP8, and this flow plays only a secondary role in the HPE. This shows that the effect of the sea state on the heat exchanges in systems leading to HPEs is likely very small.

This study of the sensitivity to wave impact uses an atmospheric model at high resolution forced by realistic modelled sea states. The conclusion of this part of our study would probably be different if the simulation was carried out using a full coupling between the atmospheric and the wave model.

Acknowledgements

The authors acknowledge Météo-France and the HyMeX programme for supplying the data, sponsored by Grants MISTRALS/HyMeX and ANR-11-BS56-0005 IODA-MED project. The authors thank the HyMeX database teams (ESPRI/IPSL and SEDOO/Observatoire Midi-Pyrénées) for their help in accessing the data, as well as all SOP1 field teams who performed measurements during this time, the MeteoCat service for performing high-resolution radiosoundings in Barcelona, the AEMET service for performing high-resolution radiosoundings in Murcia, EUMETSAT and SATMOS for supplying the SEVIRI onboard Meteosat Second Generation 2 infrared channel brightness temperature data, and EUMETSAT and the KNMI scatterometer team for providing the ASCAT surface wind images. The authors are also grateful to C. Lac, G. Tanguy and F. Duffourg (Météo-France, CNRM) for their help with the modelling part. The PCIM (Pôle de Calcul Intensif pour la Mer) support team is acknowledged for providing the corresponding computing facility. The authors are also grateful to two anonymous reviewers for improving the quality of this paper.

References

- 628 Ardhuin F, Rogers E, Babanin AV, Filipot JF, Magne R, Roland A, Van Der Westhuysen A,
629 Queffelec P, Lefevre JM, Aouf L, Collard F. 2010. Semiempirical dissipation source
630 functions for ocean waves. Part I: Definition, calibration, and validation. *J. Phys.*
631 *Oceanography*, **40**(9): 1917–1941, doi:10.1175/2010JPO4324.1.
- 632 Barthlott C, Kirshbaum DJ. 2013. Sensitivity of deep convection to terrain forcing over
633 Mediterranean islands. *Q. J. R. Meteorol. Soc.* **139**: 1762–1779, doi:10.1002/qj.2089.
- 634 Berthou S, Mailler S, Drobinski P, Arsouze T, Bastin S, Béranger K, Flaounas E, Lebeaupin
635 Brossier C, Somot S, Stéfanon M. 2016. Influence of submonthly air–sea coupling on heavy
636 precipitation events in the Western Mediterranean basin. *Q.J.R. Meteorol. Soc.* **142**: 453–471,
637 doi:10.1002/qj.2717.
- 638 Bougeault P, Lacarrère P. 1989. Parameterization of orography-induced turbulence in a meso-beta-
639 scale model. *Mon. Weather Rev.* **117**: 1872–1890.
- 640 Bresson E, Ducrocq V, Nuissier O, Ricard D, de Saint-Aubin C. 2012. Idealized numerical study of
641 Southern France heavy precipitating events: Identification of favouring ingredients. *Q. J. R.*
642 *Meteorol. Soc.* **138**: 1751–1763.
- 643 Buzzi A, Davolio S, Malguzzi P, Drofa O, Mastrangelo D. 2014. Heavy rainfall episodes over
644 Liguria in autumn 2011: numerical forecasting experiments. *Nat. Hazards Earth Syst. Sci.* **14**:
645 1325–1340 doi:10.5194/nhess-14-1325-2014.
- 646 Caniaux G, Redelsperger JL, Lafore JP. 1994. A numerical study of the stratiform region of a fast-
647 moving squall line. *J. Atmos. Sci.* **51**: 2046–2074.
- 648 Cuxart J, Bougeault P, Redelsperger JL. 2000. A turbulence scheme allowing for mesoscale and
649 large-eddy simulations. *Q. J. R. Meteorol. Soc.* **126**: 1–30, doi: 10.1002/qj.49712656202.
- 650 Davolio S, Volonté A, Manzato A, Pucillo A, Cicogna A, Ferrario ME. 2016. Mechanisms
651 producing different precipitation patterns over north-eastern Italy: insights from HyMeX-

1
2
3
4
5
6
7
8
9
10
11
12
13
14
15
16
17
18
19
20
21
22
23
24
25
26
27
28
29
30
31
32
33
34
35
36
37
38
39
40
41
42
43
44
45
46
47
48
49
50
51
52
53
54
55
56
57
58
59
60

SOP1 and previous events. *Q.J.R. Meteorol. Soc.* **142**: 188–205, doi:10.1002/qj.2731.

Di Muzio E. 2014. ‘Climatological characterization and dynamics of barrier winds in the Italian region’, PhD thesis. <http://amslaurea.unibo.it/6688> (accessed 2 October 2016).

Donlon CJ, Martin M, Stark JD, Roberts-Jones J, Fiedler E, Wimmer W. 2012. The operational sea surface temperature and sea ice analysis (OSTIA) system. *Remote Sens. Environ.* **116**: 140–158, doi:10.1016/j.rse.2010.10.017 2011.

Drobinski P, Ducrocq V, Alpert P, Anagnostou E, Béranger K, Borga M, Braud I, Chanzy A, Davolio S, Delrieu G, Estournel C, Filali Boubrahmi N, Font J, Grubisic V, Gualdi S, Homar V, Ivanan-Picek B, Kottmeier C, Kotroni V, Lagouvardos K, Lionello P, Llasat MC, Ludwig W, Lutoff C, Mariotti A, Richard E, Romero R, Rotunno R, Roussot O, Ruin I, Somot S, Taupier-Letage I, Tintoré J, Uijlenhoet R, Wernli H. 2014. HyMeX: A 10-year multidisciplinary program on the Mediterranean water cycle. *Bull. Am. Meteorol. Soc.* **95**: 1063–1082, doi:10.1175/BAMS-D-12-00242.1.

Ducrocq V, Nuissier O, Ricard D. 2008. A numerical study of three catastrophic precipitating events over Southern France. Part II: Mesoscale triggering and stationarity factors. *Q. J. R. Meteorol. Soc.* **134**: 131–145, doi:10.1002/qj.199.

Ducrocq V, Braud I, Davolio S, Ferretti R, Flamant C, Jansà A, Kalthoff N, Richard E, Taupier-Letage I, Ayrat PA, Belamari S, Berne A, Borga M, Boudevillain B, Bock O, Boichard JL, Bouin MN, Bousquet O, Bouvier C, Chiggiato J, Cimini D, Corsmeier U, Coppola L, Cocquerez P, Defer E, Delano J, Di Girolamo P, Doerenbecher A, Drobinski P, Dufournet Y, Fourrié N, Gourley JJ, Labatut L, Lambert D, Le Coz J, Marzano FS, Molinié G, Montani A, Nord G, Nuret M, Ramage K, Rison B, Roussot O, Said F, Schwarzenboeck A, Testor P, Van Baelen J, Vincendon B, Aran M, Tamayo J. 2014. HyMeX-SOP1: The field campaign dedicated to heavy precipitation and flash flooding in the Northwestern Mediterranean. *Bull.*

- 676 *Am. Meteorol. Soc.* **95**: 1083–1100, doi:10.1175/BAMS-D-12-00244.1.
- 677 Ducrocq V, Davolio S, Ferretti R, Flamant C, Santaner VH, Kalthoff N, Richar E, Wernli H. 2016.
- 678 Editorial. Introduction to the HyMeX Special Issue on 'Advances in understanding and
- 679 forecasting of heavy precipitation in Mediterranean through the HyMeX SOP1 field
- 680 campaign', *Q.J.R. Meteorol. Soc.*, **142**(1): 1-6, doi:10.1002/qj.2856.
- 681 Duffourg F, Nuissier O, Ducrocq V, Flamant C, Chazette P, Delanoë J, Doerenbecher A, Fourrié N,
- 682 Di Girolamo P, Lac C, Legain D, Martinet M, Saïd F, Bock O. 2016. Offshore deep
- 683 convection initiation and maintenance during the HyMeX IOP 16a heavy precipitation event.
- 684 *Q.J.R. Meteorol. Soc.* **142**: 259–274, doi:10.1002/qj.2725.
- 685 Fairall CW, Bradley EF, Hare JE, Grachev AA, Edson JB. 2003. Bulk parameterization of air-sea
- 686 fluxes: Updates and verification for the COARE algorithm. *J. Clim.* **16**: 571–591.
- 687 Fourrié N, Bresson E, Nuret M, Jany C, Brousseau P, Doerenbecher A, Kreitz M, Nuissier O,
- 688 Sevault E, Bénichou H, Amodei M, Pouponneau F. 2015. AROME-WMED, a real-time
- 689 mesoscale model designed for the HyMeX special observation periods. *Geosci. Model Dev.* **8**:
- 690 1919–1941, doi:10.5194/gmd-8-1919-2015.
- 691 Gal-Chen T, Somerville RCJ. 1975. On the use of a coordinate transformation for the solution of the
- 692 Navier–Stokes equations. *J. Comput. Phys.* **17**: 209–228, doi: 10.1016/0021-9991(75) 90037-
- 693 6.
- 694 Hanssen AW, Kuipers WJA. 1965. 'On the relationship between the frequency of rain and various
- 695 meteorological parameters: with reference to the problem of objective
- 696 forecasting'. Wageningen UR Library: Wageningen, Holland.
- 697 Hare JE, Persson POG, Fairall CW, Edson JB. 1999. 'Behavior of Charnock's relationship for high
- 698 wind conditions', *Proc. 13th Symp. on Bound. Layers and Turbulence*. American Meteorol.
- 699 Soc.: Dallas, TX, pp 252–255.

1
2
3
4
5
6
7
8
9
10
11
12
13
14
15
16
17
18
19
20
21
22
23
24
25
26
27
28
29
30
31
32
33
34
35
36
37
38
39
40
41
42
43
44
45
46
47
48
49
50
51
52
53
54
55
56
57
58
59
60

Jansà A, Campins J, Picornell MA, Guijarro JA. 2014. Heavy rain and strong wind events over Spain during HyMeX SOP1. *Thetys, Journal of Mediterranean Meteorology and Climatology* **11**: 25–38.

Khodayar S, Raff F, Kalthoff N, Bock O. 2016. Diagnostic study of a high-precipitation event in the Western Mediterranean: adequacy of current operational networks. *Q.J.R. Meteorol. Soc.*, **142**: 72–85, doi:10.1002/qj.2600.

Lafore JP, Stein J, Asencio N, Bougeault P, Ducrocq V, Duron J, Fischer C, Hèreil P, Mascart P, Masson V, Pinty JP, Redelsperger JL, Richard E, Vilà- Guerau de Arellano J. 1998. The Meso-NH atmospheric simulation system. Part I: Adiabatic formulation and control simulations. *Ann. Geophys.* **16**: 90–109, doi: 10.1007/s00585-997-0090-6.

Llasat MC, Llasat-Botija M, Petrucci O, Pasqua AA, Rossell J, Vinet F, Boissier L. 2013. Towards a database on societal impact of Mediterranean floods within the framework of the HyMeX project. *Nat. Hazards Earth Syst. Sci.* **13**: 1337–1350, doi: 10.5194/nhess-13-1337-2013.

Masson V, Le Moigne P, Martin E, Faroux S, Alias A, Alkama R, Belamari S, Barbu A, Boone A, Bouyssel F, Brousseau P, Brun E, Calvet JC, Carrer D, Decharme B, Delire C, Donier S, Essaouini K, Gibelin AL, Giordani H, Habets F, Jidane M, Kerdraon G, Kourzeneva E, Lafaysse M, Lafont S, Lebeaupin-Brossier C, Lemonsu A, Mahfouf J-F, Marguinaud P, Mokhtari M, Morin S, Pigeon G, Salgado R, Seity Y, Taillefer F, Tanguy G, Tulet P, Vincendon B, Vionnet V, Voldoire A. 2013. The SURFEXv7.2 land and ocean surface platform for coupled or offline simulation of Earth surface variables and fluxes. *Geosci. Model Dev.* **6**: 929–960, doi: 10.5194/gmd-6-929-2013.

Miglietta M, Rotunno R. 2010. Numerical simulations of low-CAPE flows over a mountain ridge. *J. Atmos. Sci.* **67**: 2391–2401, doi: 10.1175/2010JAS3378.1.

Miglietta MM, Rotunno R. 2012. Application of theory to observed cases of orographically forced

- convective rainfall, *Mon. Weather Rev.* **140**: 3039–3053.
- Nuissier O, Ducrocq V, Ricard D. 2008. A numerical study of three catastrophic precipitating events over Southern France. Part I: Numerical framework and synoptic ingredients. *Q. J. R. Meteorol. Soc.* **134**: 111–130, doi: 10.1002/qj.200.
- Nuissier O, Joly B, Joly A, Ducrocq V, Arbogast P. 2011. A statistical downscaling to identify the large-scale circulation patterns associated with heavy precipitation events over Southern France. *Q. J. R. Meteorol. Soc.* **137**: 1812–1827, doi: 10.1002/qj.866.
- Oost WA, Komen GJ, Jacobs CMJ, Van Oort C. 2002. New evidence for a relation between wind stress and wave age from measurements during ASGAMAGE. *Boundary-Layer Meteorol.* **103**: 409–438, doi: 10.1023/A:1014913624535.
- Pinty JP, Jabouille P. 1998. 'A mixed-phased cloud parametrization for use in a mesoscale non-hydrostatic model: Simulations of a squall line and of orographic precipitation'. In *Proceedings of the Conference on Cloud Physics*, 17–21 August, Everett, WA: 217–220. American Meteorological Society: Boston.
- Ricard D, Ducrocq V, Auger L. 2012. A climatology of the mesoscale environment associated with heavily precipitating events over a northwestern Mediterranean area. *J. Appl. Meteorol. Clim.* **51**: 468–488, doi: 10.1175/JAMC-D-11-017.1.
- Röhner L, Nerding KU, Corsmeier U. 2016. Diagnostic study of a HyMeX heavy precipitation event over Spain by investigation of moisture trajectories. *Q.J.R. Meteorol. Soc.* **142**: 287–297, doi:10.1002/qj.2825.
- Schaefer JT. 1990. The critical success index as an indicator of warning skill. *Weather Forecasting* **5**: 570–575, doi: 10.1175/1520-0434(1990)005.
- Shapiro, M.A., and D. Keyser, 1990: Fronts, jet streams and the tropopause. *Extratropical Cyclones: The Erik Palmen Memorial Volume*, C., W. Newton and E. O. Holopainen, Eds.,

1
2
3
4
5
6
7
8
9
10
11
12
13
14
15
16
17
18
19
20
21
22
23
24
25
26
27
28
29
30
31
32
33
34
35
36
37
38
39
40
41
42
43
44
45
46
47
48
49
50
51
52
53
54
55
56
57
58
59
60

748 Amer. Meteor. Soc., 167-191.

749 Taillefer F. 2002. ‘CANARI (Code for the Analysis Necessary for Arpege for its Rejects and its
750 Initialization): Technical Documentation’, Technical Report. CNRM/GMAP, Groupe de
751 Modél. pour l’Assimilation et la Prévision, Cent. Nati. de Rech. Météorol., Météo-France,
752 Toulouse, France. <http://www.cnrm.meteo.fr/gmapdoc/spip.php?article3> (accessed 2 May
753 2017).

754 Thévenot O, Bouin MN, Ducrocq V, Lebeaupin Brossier C, Nuissier O, Pianezze J, Duffourg F.
755 2016. Influence of the sea state on Mediterranean heavy precipitation: a case-study from
756 HyMeX SOP1. *Q.J.R. Meteorol. Soc.*, **142**: 377–389, doi:10.1002/qj.2660.

757 Tolman H. 2014. 'User manual and system documentation of WAVEWATCH III version 4.18'.
758 Environmental Modeling Center Marine Modeling Analysis Branch.

Mean bias		SDD	Correlation r	ETS			HK		
<i>Threshold</i>				<i>5 mm</i>	<i>15 mm</i>	<i>25 mm</i>	<i>5 mm</i>	<i>15 mm</i>	<i>25 mm</i>
NOWAV	0.4	15.5	0.74	0.63	0.78	0.64	0.79	0.90	0.80
WW3_F	0.4	16.0	0.72	0.63	0.74	0.61	0.79	0.89	0.79

Table 1: Mean bias, standard deviation difference, ETS and HK scores (see text) of the NOWAV and WW3_F simulations against 24-h accumulated rain gauge observations on 28 September 2012 (mean bias and SDD in mm).

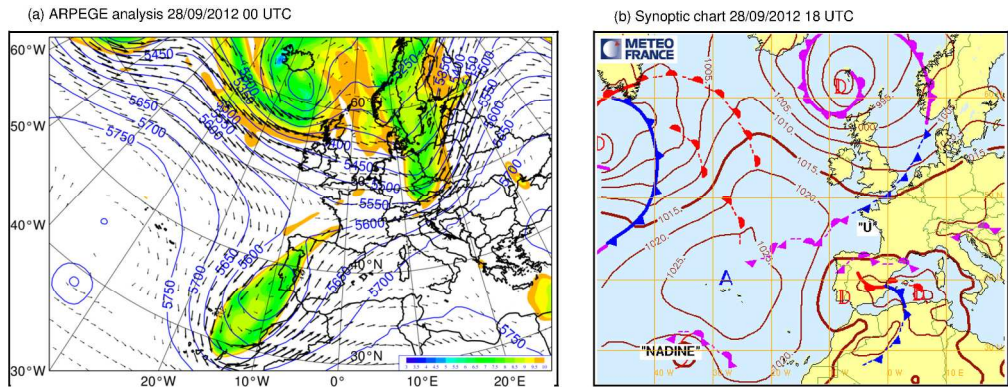


Figure 1: Synoptic conditions of the IOP8 with (a) ARPEGE analysis showing the height of potential vorticity anomaly equal to 2.0 PVU (colour chart, km), the 500 hPa geopotential (isobars, m) and the 300 hPa wind (above 10 m s⁻¹) at 0000 UTC on 28 September 2012 and (b) synoptic Meteo-France analysis with fronts and isobars, at 1800 UTC on 28 September 2012.

273x104mm (300 x 300 DPI)

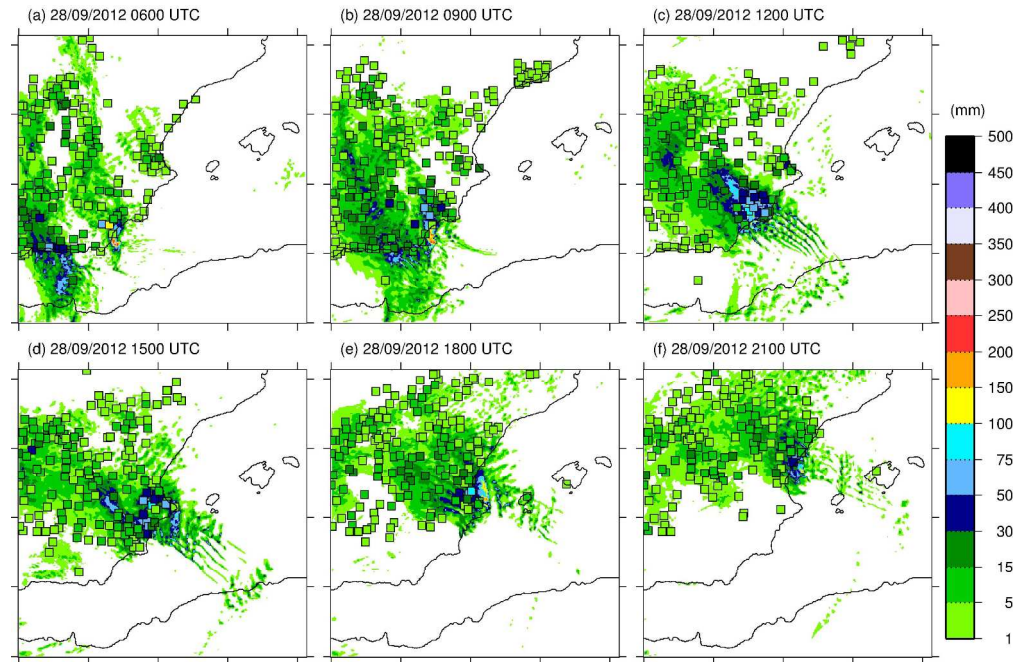


Figure 2: Three-hour cumulated rain amount from the NOWAV simulation (see Table 1 and sections 3.1 and 3.2) and measured by rain gauges (coloured squares) starting at (a) 0600 UTC, (b) 0900 UTC, (c) 1200 UTC, (d) 1500 UTC, (e) 1800 UTC and (f) 2100 UTC on 28 September 2012.

278x183mm (300 x 300 DPI)

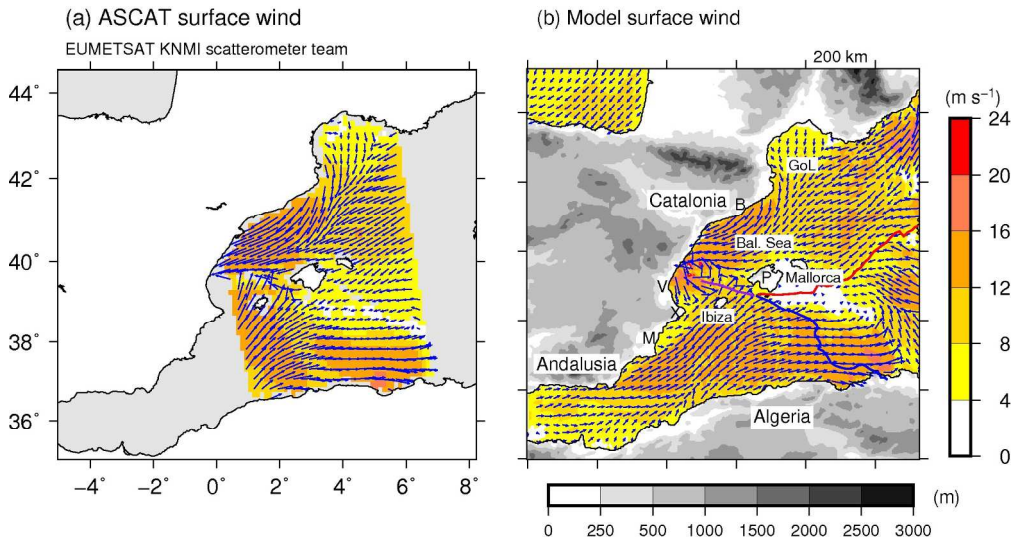


Figure 3: Sea surface wind (m s^{-1}) (a) from ASCAT onboard Metop-A between 2100 UTC on 28 September and 0000 UTC on 29 September and (b) from the NOWAV simulation (see sections 3.1 and 3.2) at 2230 UTC on 28 September 2012, with the surface fronts superimposed. V denotes Valencia, B Barcelona, M Murcia, X Xabia, and P Palma de Mallorca. The topography (grey scale, m) and main geographical areas are also indicated (b).

192x102mm (300 x 300 DPI)

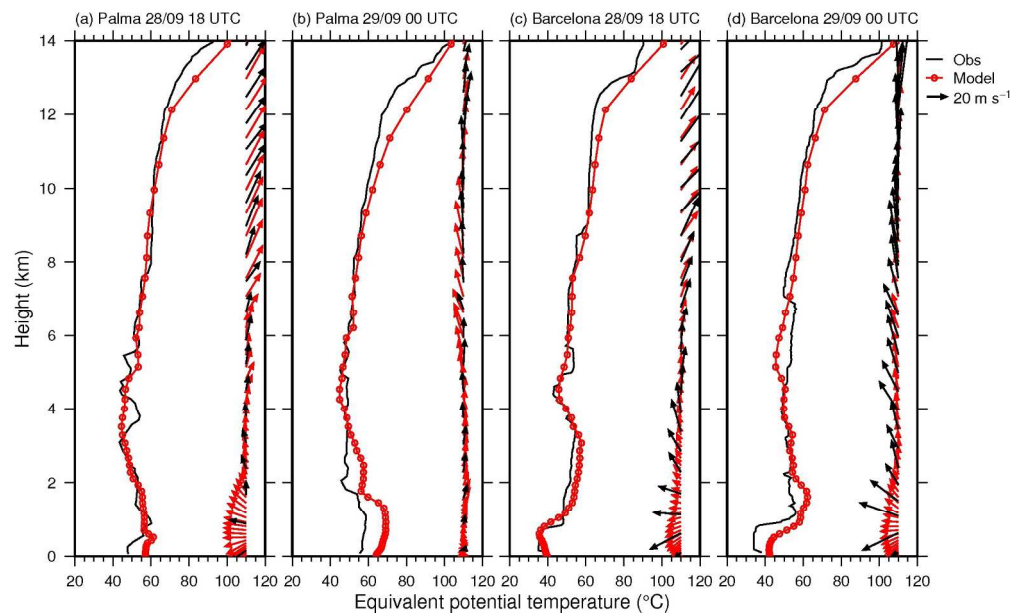


Figure 4: Vertical profiles (height in km) of equivalent potential temperature (°C) and horizontal wind (vector) from radio soundings (black) and from NOWAV simulation (red) in Palma de Mallorca (a) at 1800 UTC on 28 September 2012 and (b) at 0000 UTC on 29 September, and in Barcelona (c) at 1800 UTC on 28 September and (d) at 0000 UTC on 29 September 2012.

184x111mm (300 x 300 DPI)

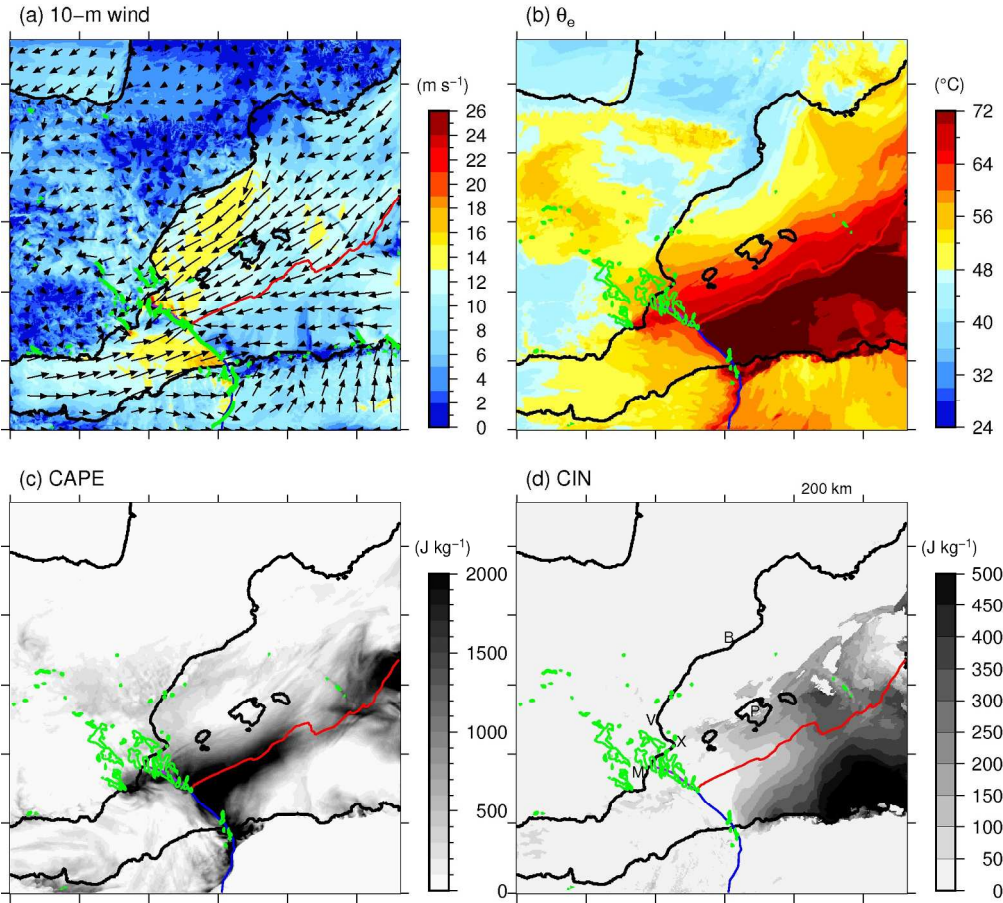


Figure 5: (a) 10-m wind (m s^{-1}), (b) equivalent potential temperature ($^{\circ}\text{C}$), (c) convective available potential energy (J kg^{-1}), and (d) convective inhibition (J kg^{-1}) from the NOWAV simulation, at 1600 UTC on 28 September 2012. The green contour in (a) indicates the moisture convergence rate above $3 \times 10^{-5} \text{ kg m}^{-3} \text{ s}^{-1}$ at the surface. The green contour in (b), (c), (d) indicates the simulated radar reflectivity at 2000 m above 40 dBz. The red (resp. blue) line indicates the warm (rep. cold) front, the purple line the occluded front. V denotes Valencia, B Barcelona, M Murcia, X Xabia, and P Palma de Mallorca.

205x185mm (300 x 300 DPI)

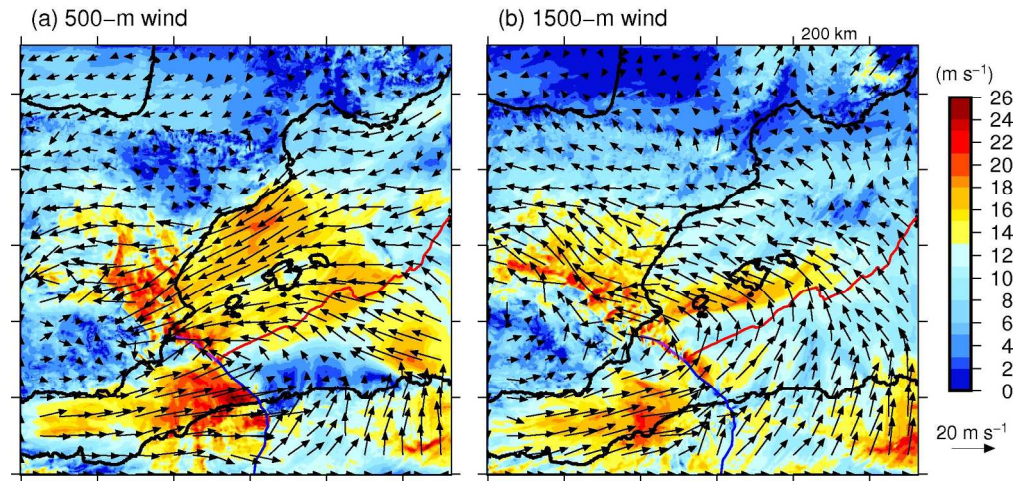


Figure 6: Wind field from the NOWAV simulation (m s^{-1}) at 1600 UTC on 28 September 2012, (a) at 500 m and (b) at 1500 m agl. The red (resp. blue) line indicates the warm (rep. cold) front, the purple line the occluded front.

186x90mm (300 x 300 DPI)

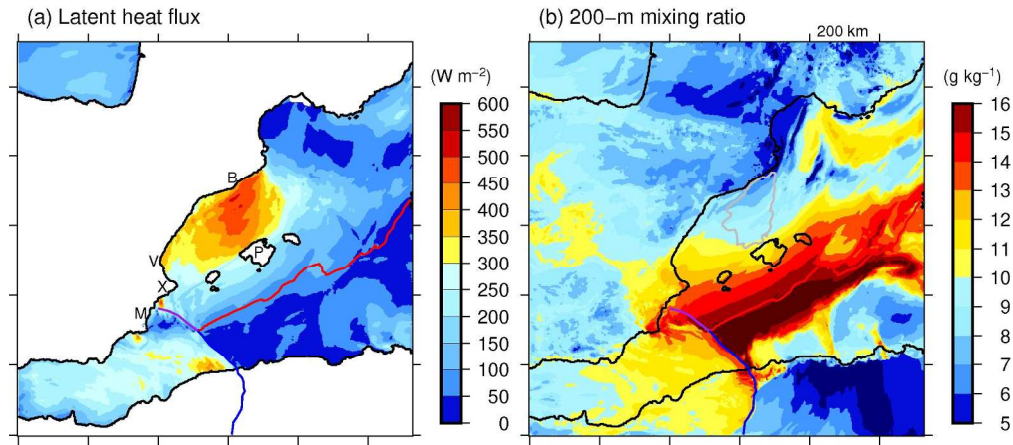


Figure 7: (a) Surface latent heat flux (W m^{-2}) and (b) mixing ratio at 200 m (g kg^{-1}) from the NOWAV simulation at 1600 UTC on 28 September 2012. The grey contour in (b) indicates the area with surface evaporation above 400 W m^{-2} . The red (resp. blue) line indicates the warm (rep. cold) front, the purple line the occluded front. V denotes Valencia, B Barcelona, M Murcia, X Xabia, and P Palma de Mallorca.

203x90mm (300 x 300 DPI)

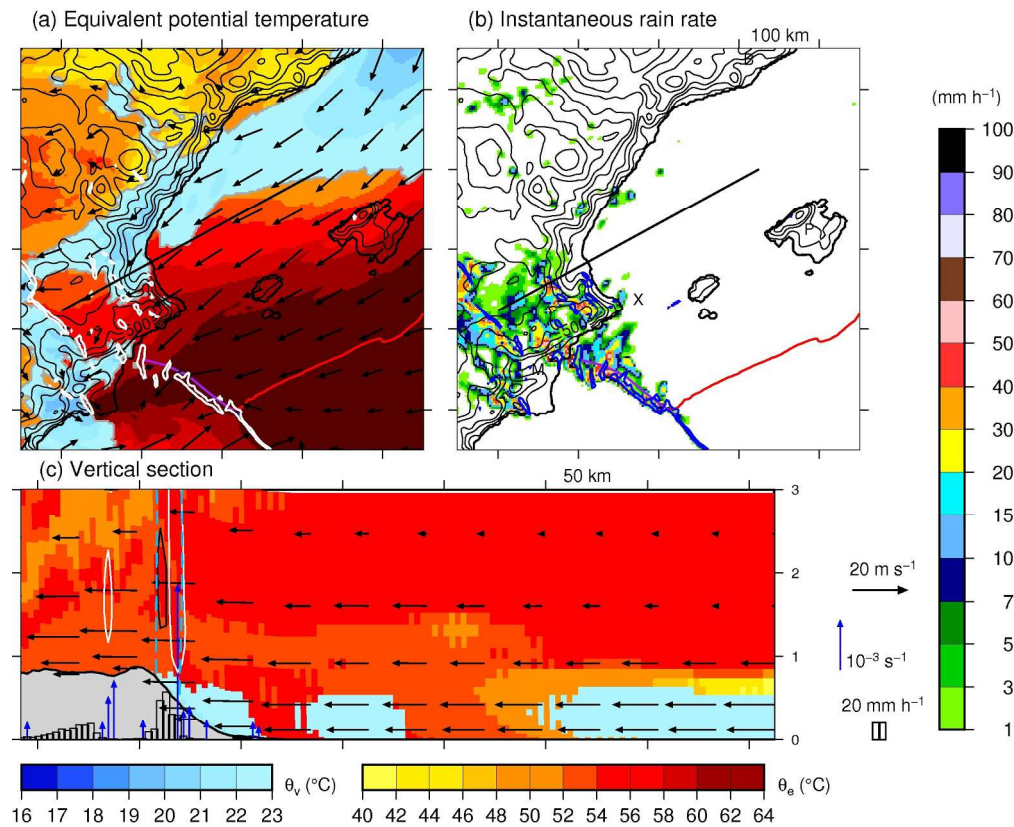


Figure 8: (a) Equivalent potential temperature and virtual potential temperature at the surface (°C, colour scale), 10-m wind (vectors), and vertical velocities above 1 m s⁻¹ at 500 m agl (white contour); (b) Instantaneous rain rate (mm h⁻¹, colour scale), and moisture convergence rate above 3 10⁻⁵ kg m⁻³ s⁻¹ at the surface (blue contour); (c) vertical profiles of the equivalent potential temperature and virtual potential temperature (°C, colour scale ; height scale in km), projection of the wind (black arrows), instantaneous rain rate (vertical bars), vertical velocities above 1 m s⁻¹ (white contour) or below -1 m s⁻¹ (black contour), cloud precipitating water above 1 g kg⁻¹ (light blue, dashed contour), and horizontal convergence at 120 m agl (blue arrows) from the NOWAV simulation at 1600 UTC on 28 September 2012. The black line in (a) indicates the vertical cross section used in (c). The virtual potential temperature in (a) and (c) replaces the equivalent potential temperature when under 23°C to indicate cold pools. The red (resp. blue) line in (a) and (b) indicates the warm (rep. cold) front, the purple line indicates the occluded front. V denotes Valencia, B Barcelona, M Murcia, X Xabia, and P Palma de Mallorca.

199x163mm (300 x 300 DPI)

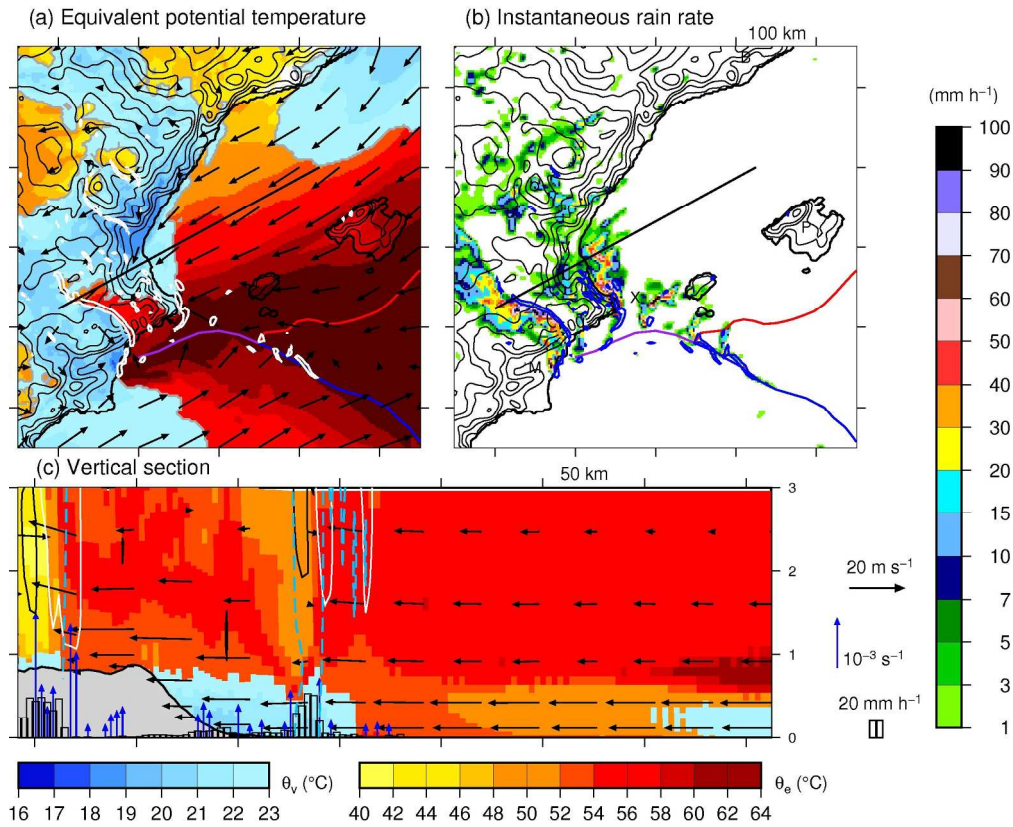


Figure 9: Same as Figure 8, but at 1830 UTC on 28 September 2012.

199x163mm (300 x 300 DPI)

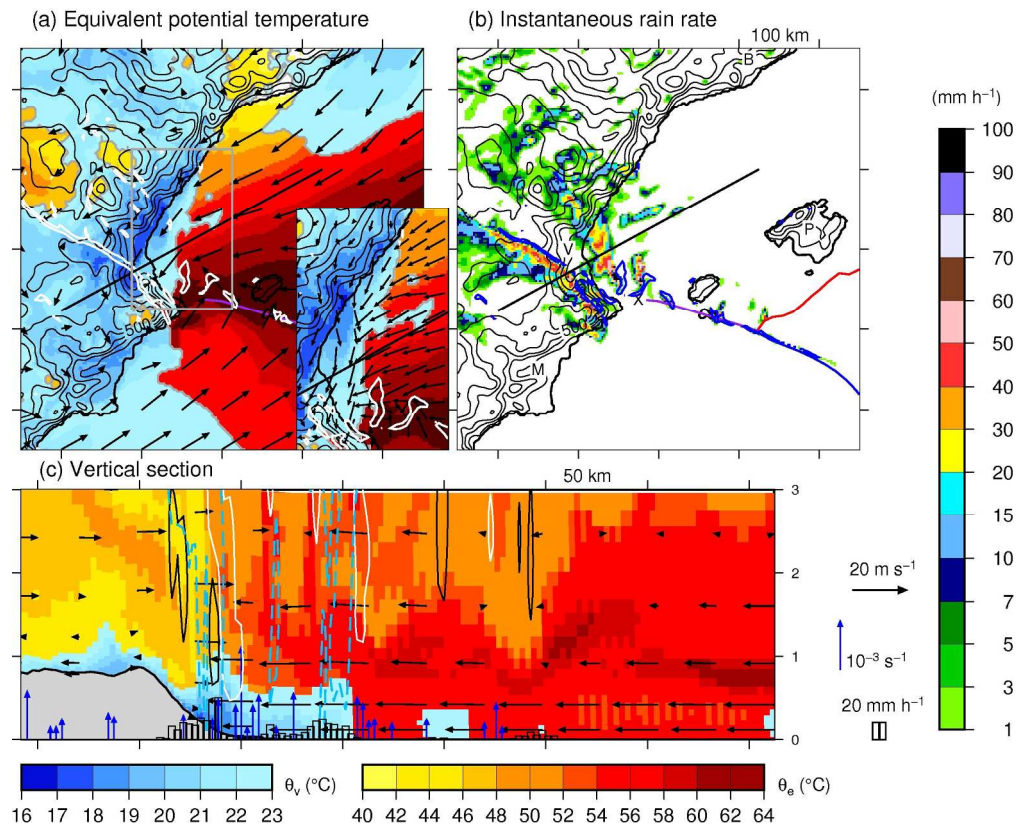


Figure 10: Same as Figure 8, but at 2000 UTC on 28 September 2012. The insert in (a) (grey frame) represents in more details the 10-m wind field on the coast at the level of Valencia.

199x163mm (300 x 300 DPI)

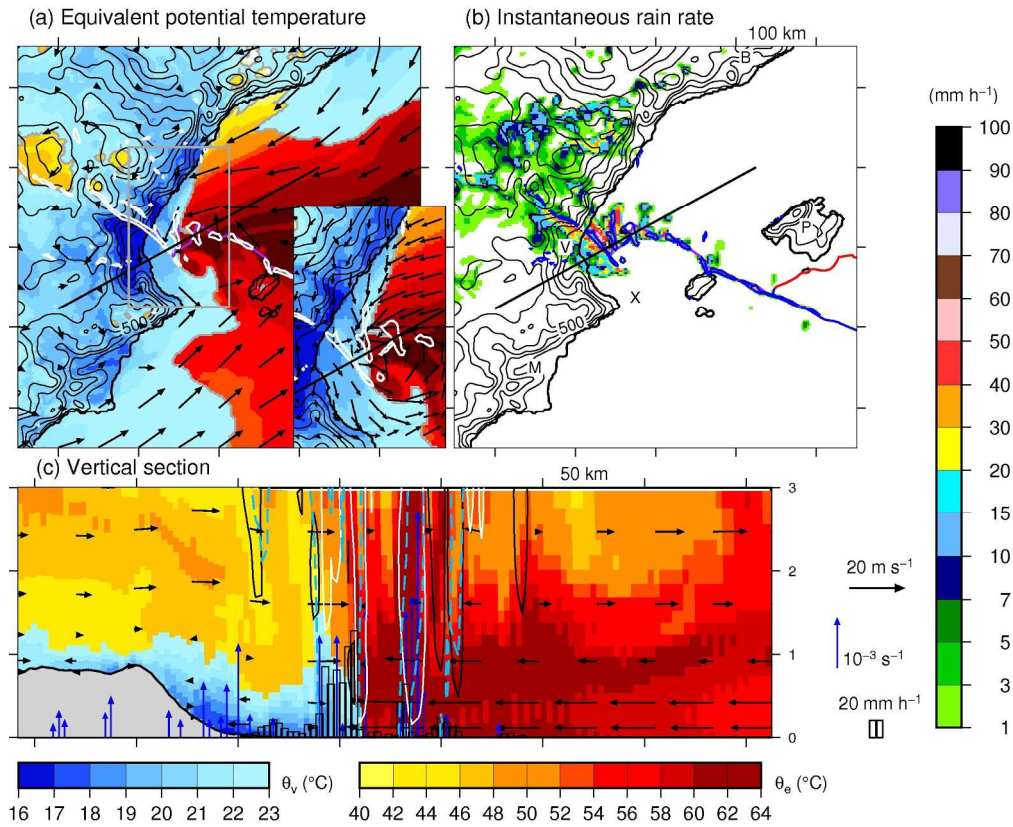


Figure 11: Same as Figure 10, but at 2130 UTC on 28 September 2012.

199x163mm (300 x 300 DPI)

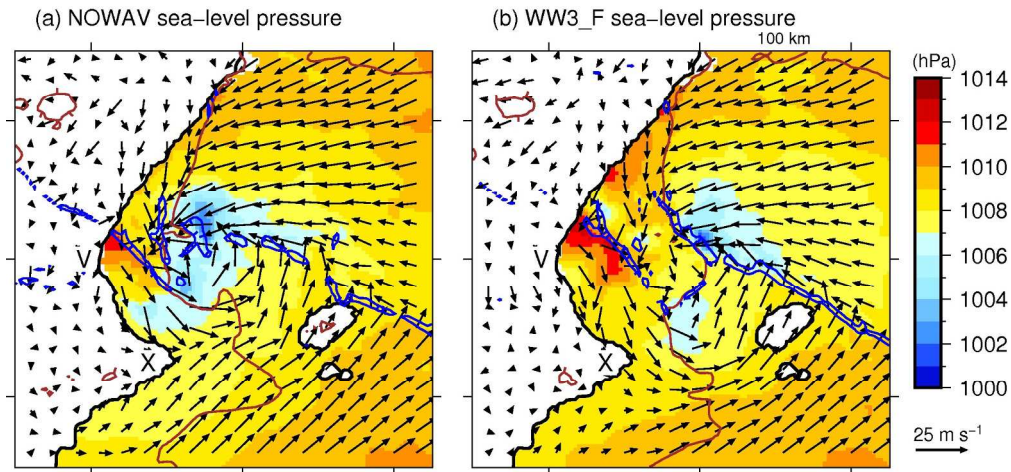


Figure 12: Sea-level pressure (colour scale, hPa), surface wind (black arrows), cold pool edges as identified by $\theta_v \leq 23^\circ\text{C}$ (brown contour), and areas of moisture convergence rate above $3 \times 10^{-5} \text{ kg m}^{-3} \text{ s}^{-1}$ at the surface (blue contour) from the (a) NOWAV and (b) WW3_F simulations at 2130 UTC, on 28 September 2012. V denotes Valencia, and X Xabia.

192x91mm (300 x 300 DPI)

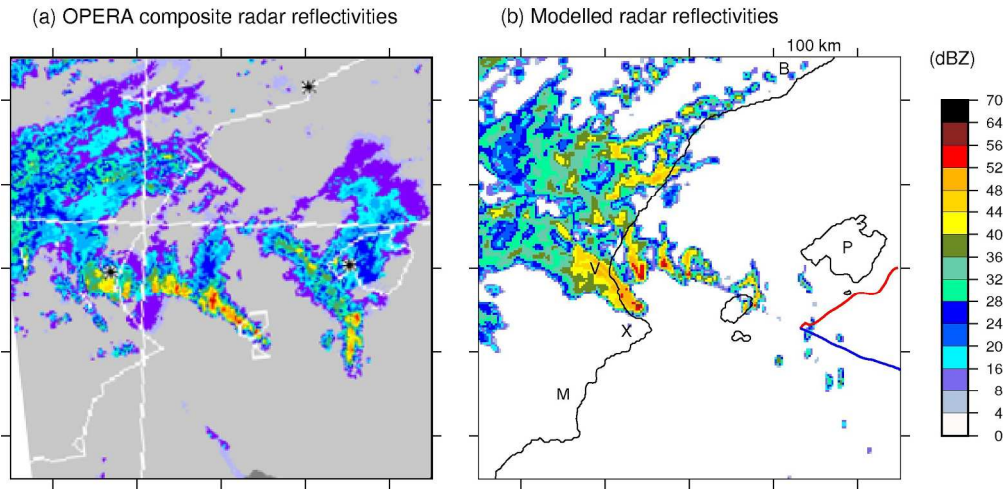


Figure 13: Radar reflectivities (dBZ) at 2000 m agl in the Valencia region at 2100 UTC on 28 September 2012 (a) from the Odyssey composite product, and (b) from the NOWAV simulation. The red (resp. blue) line indicates the warm (rep. cold) front. V denotes Valencia, B Barcelona, M Murcia, X Xabia, and P Palma de Mallorca.

190x92mm (300 x 300 DPI)

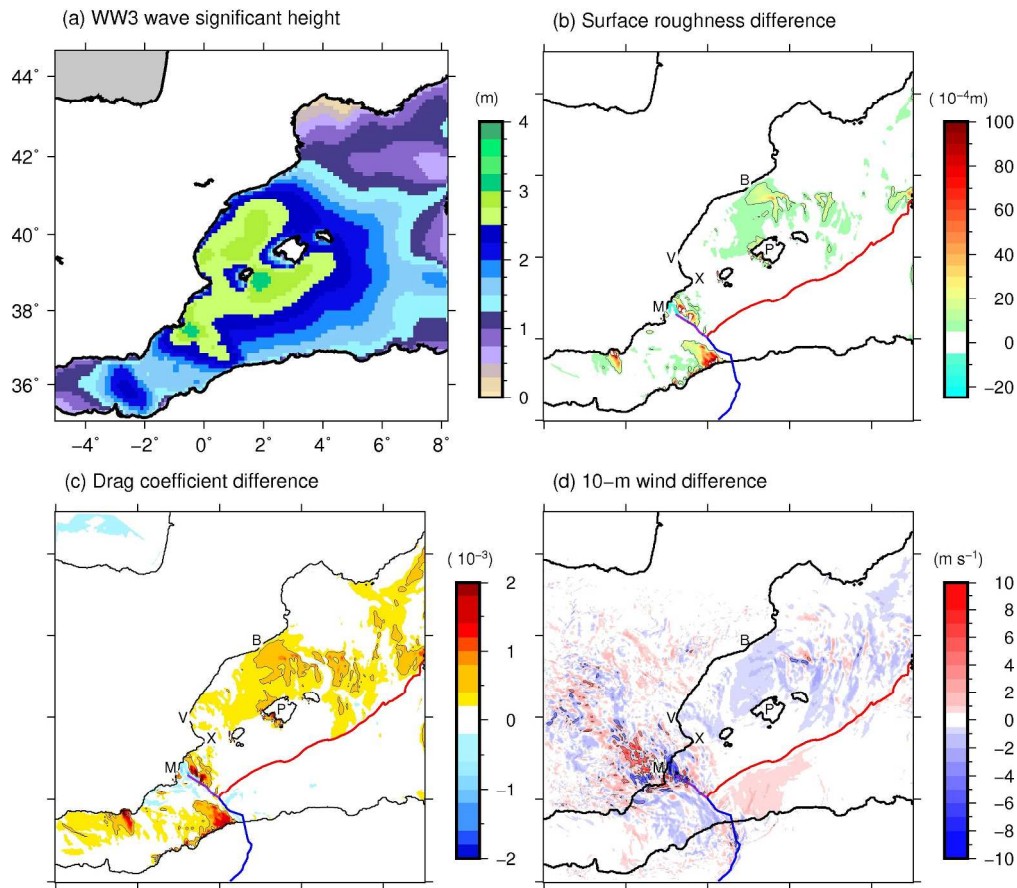


Figure 14: (a) Wave significant height from the Wavewatch III® model outputs (m), (b) surface roughness length difference (10^{-4} m), (c) drag coefficient difference (10^{-3}) and (d) 10-m wind speed difference (m s^{-1}) between the WW3_F and NOWAV simulations at 1500 UTC on 28 September 2012. The red (resp. blue) line indicates the warm (rep. cold) front, the purple line the occluded front. V denotes Valencia, B Barcelona, M Murcia, X Xabia, and P Palma de Mallorca.

217x192mm (300 x 300 DPI)

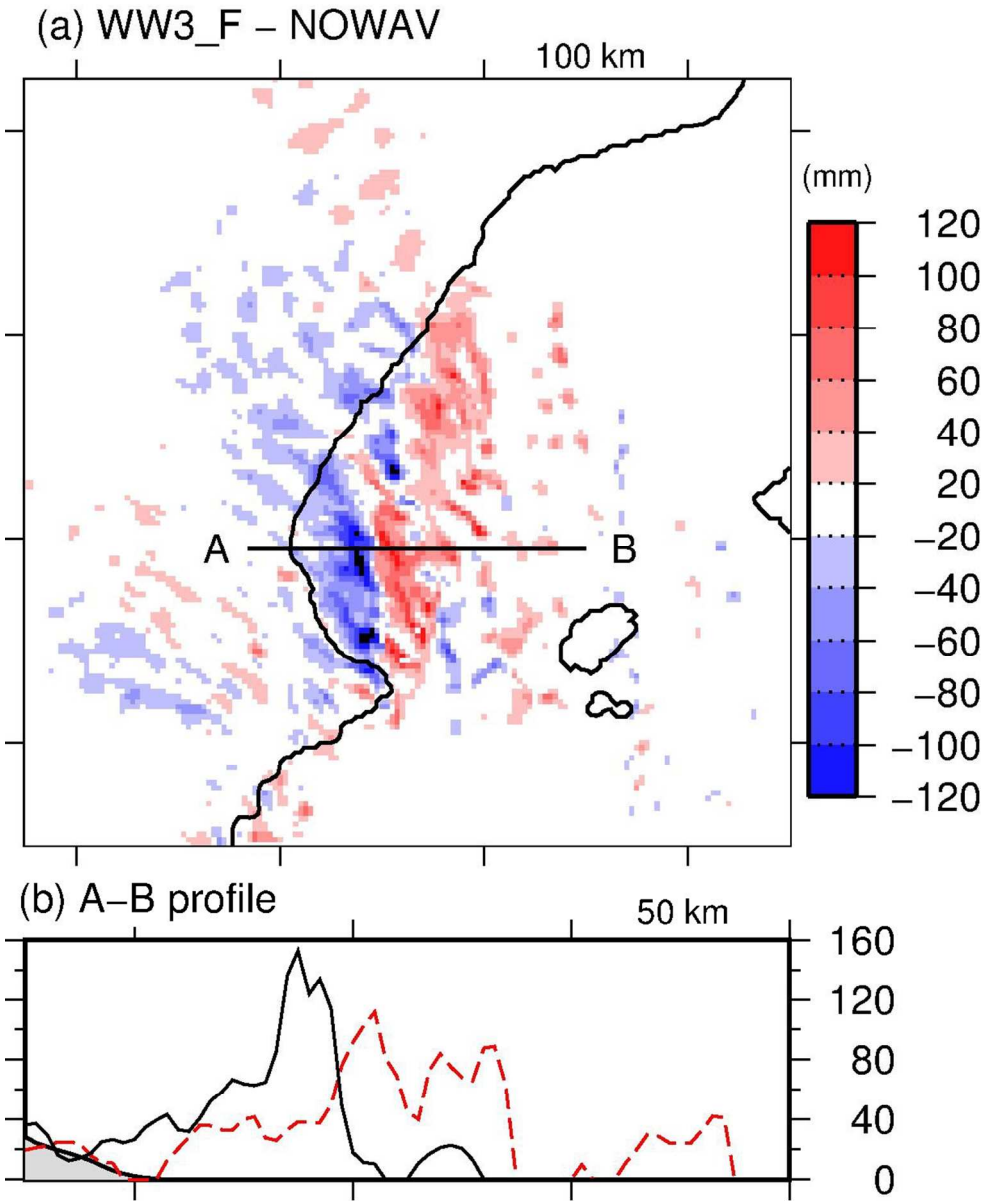


Figure 15: (a) Six-hour cumulated rain difference (mm) between the WW3_F and NOWAV simulations, and (b) six-hour cumulated rain (mm) in the NOWAV (black solid line) and WW3_F (red dashed line) along the A-B profile between 1800 UTC on 28 September 2012 and 0000 UTC on 29 September 2012.

102x125mm (300 x 300 DPI)

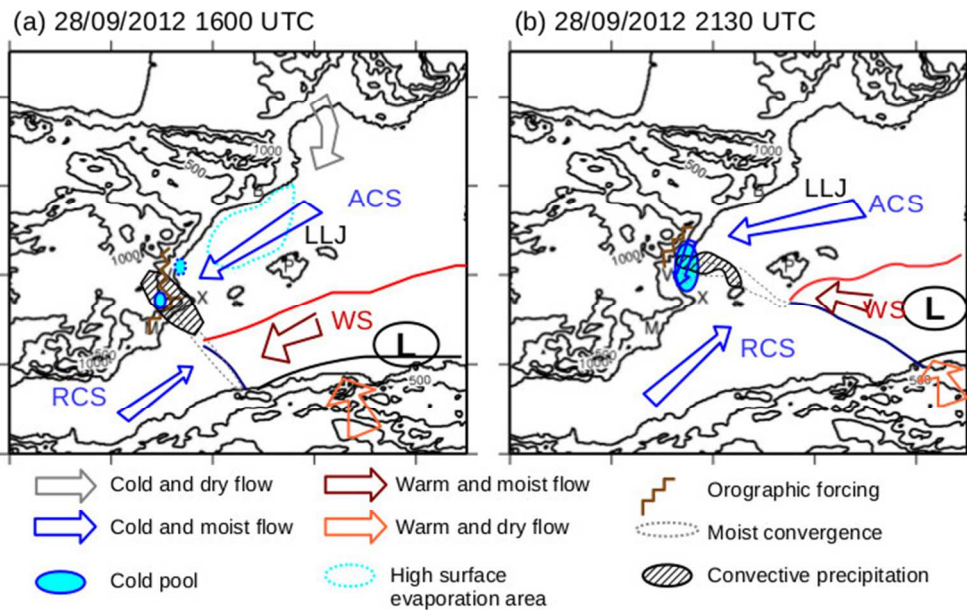


Figure 16: Schemes of the low-level flows and forcing mechanisms resulting in heavy precipitation on the Murcia-Valencia region (a) at 1600 UTC and (b) at 2130 UTC on 28 September 2012. The surface cold (warm) front is indicated with a blue (red) line. LLJ corresponds to low-level jet, ACS to ahead cold sector, WS to warm sector and RCS to rear cold sector.

186x114mm (100 x 100 DPI)

Processes leading to deep convection and sensitivity to sea-state representation during HyMeX IOP8 heavy precipitation event, M.-N. Bouin *, J.-L. Redelsperger, and C. Lebeaupin Brossier

Using numerical simulations, the processes leading to deep convection ad heavy precipitation during the HyMeX-SOP1 IOP8 are investigated. Cold pools and associated inflow deflection play a key role in positioning heavy precipitation, in addition to orographic effects and moisture convergence at sea. Representing in a more realistic way the sea surface roughness results in a displacement of the rain patterns of 50 km offshore.

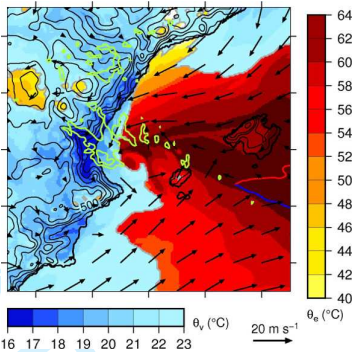


Figure caption: Equivalent potential temperature (°C) and virtual potential temperature (°C) at the surface as a proxy of cold pools, 10-m wind field (arrows) and convective precipitation (green contour) in northeastern Spain at 2130 UTC on the 28 September 2012.